Ten years of marine current measurements in Espartel Sill, Strait of Gibraltar

S. Sammartino[1], J. García Lafuente[1], C. Naranjo[1], J.C. Sánchez Garrido[1], R. Sánchez Leal[2], A. Sánchez Román[3]

[1]*Physical Oceanography Group, University of Málaga, Campus de Teatinos s/n, 29071, Málaga, Spain*
[2]*Spanish Institute of Oceanography (IEO), Cadiz Oceanography Center, Cádiz, Spain*
[3]*Mediterranean Institute for Advanced Studies (IMEDEA), Esporles, Spain*

Corresponding author: Simone Sammartino, ssammartino@ctima.uma.es, Physical Oceanography Group, University of Málaga, Campus de Teatinos s/n, 29071, Málaga, Spain

Key points

- A ten-year series of ADCP measurements has been processed.
- The series has been submitted to a careful quality control.
- The mean value of the outflow is -0.85 Sv plus/minus 0.03 Sv.

Abstract

More than ten-year of Acoustic Doppler Current Profiler observations collected at the westernmost sill (Espartel sill) of the Strait of Gibraltar by a monitoring station, have been carefully processed to provide the most updated estimation of the Mediterranean outflow. A comprehensive quality control of the factors affecting the uncertainty of the measurements has been carried out and great care has been paid to infer the current at the bottom layer, where direct observations are lacking. The mean outflow in the southern channel of the sill section has been estimated as -0.82 Sv (1 Sv = $1x10^6$ m^3 s^{-1}), with an average contribution of the eddy fluxes of -0.04 Sv. This figure is an overestimation, as the mooring measurements, assumed valid for the whole section, ignore the lateral friction. On the other hand, it only gives the flow through the southern channel and disregards the fraction flowing through shallower northern part. Both drawbacks have been addressed by investigating the cross-strait structure of the outflow from hindcasts produced by the MITgcm numerical model, run in a high-resolution domain covering the Gulf of Cádiz and Alboran Sea basins. An overall rectifying factor of 1.039 was found satisfactory to correct the first estimate, so that the final mean outflow computed from this dataset is -0.85 Sv, complemented with an uncertainty of ±0.03 Sv based on the interannual variability of the series. The temporal analysis of the series shows an outflow seasonality of around the 8% of the mean value, with maximum outflow in early spring.

Index terms: 0520, 4262, 4277, 4227

1 Introduction

The Strait of Gibraltar (SoG hereinafter) is a key location for the vigorous exchange between the Mediterranean Sea and the Atlantic Ocean that it holds. Besides a classic problem in oceanography, the dynamic of the exchange is a challenging issue due to the highly irregular topography with steeps sills and canyons (Figure 1) that interact with tidal currents of remarkable strength [*Lacombe and Richez*, 1982; *Armi and Farmer*, 1988; *Candela et al.*, 1990; *Bryden et al.*, 1994; *García Lafuente et al.*, 2000; *Sannino et al.*, 2004; *Sánchez Román et al.*, 2009; *Sánchez Garrido et al.*, 2011]. On the other hand, the influence of the exchange reaches far beyond the reduced dimensions of the strait: it is the only gateway for the renewal of the Mediterranean Sea waters and, moreover, it represents a source of high salinity water for the North Atlantic Ocean, whose fate and possible role in the thermohaline circulation of the world ocean is controversial [*Reid*, 1979; *Rahmstorf*, 1998; *New et al.*, 2001; *Rogerson et al.*, 2006]. It is not surprising, therefore, that the SoG is one of the most and exhaustively studied areas of the planet. And among the different topics of research, the estimation of the size of the exchanged flows and the assessment of their variability at different time scales are of the greatest interest for a wide variety of oceanographic issues.

Attempts to provide a reliable figure of these flows can be traced back to the beginning of the 20th century (see Table 1). They can be sorted out in three categories. Within the first one are those established on theoretical considerations, basically the volume and salt conservation for the Mediterranean, which requires the knowledge of the salinity difference between the connected water bodies and the net evaporation over the Mediterranean basin. More sophisticated theoretical approaches include energy considerations that bring the problem to the field of the hydraulics [*Bryden and Stommel*, 1984; *Armi and Farmer*, 1985; 1988; *Bryden and Kinder*, 1991].

The second category gathers the attempts based on observations, whose history is more recent due to the formidable challenge of deploying scientific instrumentation in such a harsh environment (see

white rows references in Table 1). The third group includes the outputs provided by numerical models [*Sannino et al.*, 2004; 2007; *Sánchez Garrido et al.*, 2011; *Peliz et al.*, 2013; *Boutov et al.*, 2014] whose reliability is more arguable since the models require feedback from the observations to be calibrated. Table 1 shows the values for the exchange provided by the first two categories and illustrates how the theoretically-based estimations are systematically larger than those based on observations. The latter also show a tendency to lower values as the date they were performed approaches the present days. Estimations from numerical models are not included because, in the end, they depend on the calibration of the model that in turn relies on the observations used to do it.

Table 1 – Estimations of inflow and outflow through the SoG published in literature. Gray-shaded rows indicate estimations based on theoretical considerations (salt and volume conservation, and, eventually, hydraulically controlled flows), whereas the remaining values are based on observations.

Reference	Inflow (Sv)	Outflow (Sv)
Nielsen [1912]	1.87	-1.78
Schott [1915]	1.74	-1.64
Sverdrup et al. [1942]	1.75	-1.68
Carter [1956]	0.95	-0.91
Bethoux [1979]	1.68	-1.60
Lacombe and Richez [1982]	1.21	-1.15
Bryden and Stommel [1984]	1.67	-1.59
Bryden and Kinder [1991]	0.92	-0.88
Bryden et al. [1994]	0.73	-0.68
García Lafuente et al. [2000]	0.92	-0.87
Tsimplis and Bryden [2000]	0.78	-0.67
Baschek et al. [2001]	0.81	-0.76
Candela [2001]	1.01	-0.97
García Lafuente et al. [2002]	0.96	-0.84
Vargas et al. [2006]	0.89	-0.82
Sánchez Román et al. [2009]	---	-0.78
García Lafuente et al. [2009]	---	-0.79
Soto Navarro et al. [2010]	0.81	-0.78

The objective of the present work is to provide the most updated figures for the Mediterranean outflow based on a 10-year long time series of Acoustic Doppler Current Profiler (ADCP) data

collected at the Espartel sill (ES hereinafter) in the western section of the SoG (Figure 1). Its main improvements, with respect to previous similar studies, are based on the longer time series analyzed (it is actually the longest time series ever acquired in this area), the careful quality control of the series performed and the special attention paid to the inference of the unmeasured bottom layer current. Moreover, the model used to assess of the cross-strait structure of the flow (see Section 7.3), is a widely validated instrument, used recently to investigate the complex dynamics of the Alboran Sea [*Sánchez Garrido et al.*, 2013] and the Algeciras Bay [*Sammartino et al.*, 2014; *Sánchez Garrido et al.*, 2014], both systems strictly related to the exchange in the SoG.

The ES section gathers good conditions for monitoring the outflow: currents are canalized along a relatively narrow channel where fishing activities are relatively reduced. Moreover, the hydraulic control imposed by the topography in this section is nearly permanent [*García Lafuente et al.*, 2007; *Sannino et al.*, 2007; 2009], which simplifies the computation of the flow from currentmeter observations. On the other hand, this section is not suitable for estimating the inflow, so that the paper only addresses the computation of the outflow.

The paper is organized as follows. Next Section describes the structure and design of the monitoring station. Section 3 presents ancillary datasets used in the work to support the outflow computation. A careful quality control of the factors affecting the measurements, performed paying special attention to the uncertainty introduced by each of them, is described in Section 4. The characterization of the vertical profile of the velocity in the frictional bottom layer is extensively discussed in Section 5, while Section 6 deals with questions related to the interface between Atlantic and Mediterranean waters and the manner it is defined. The estimations of the outflow are then carried out in Section 7 and the analysis of its time variability is done in Section 8. Finally, Section 9 summarizes our findings and conclusions.

2 The mooring line

The monitoring station was installed in September 2004 in ES, at the western exit of the SoG, on a depth of approximately 360 meters (Figure 1). A summary of the successive periods of observations and servicing of the moored line is presented in Table A-1 in the Appendix.

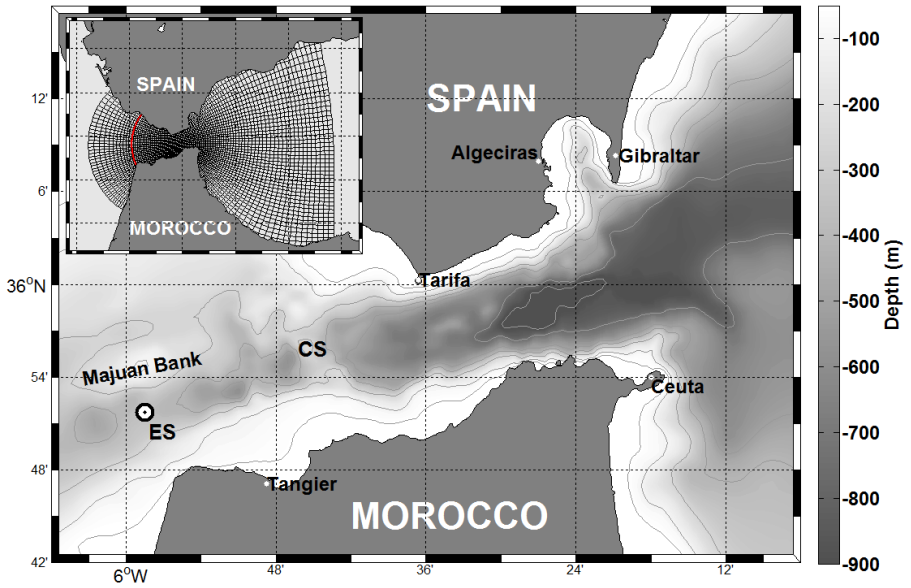

Figure 1 – Map of the Strait of Gibraltar. The moorings location is indicated by a white circle (coordinates: latitude 35° 51.71' N and Longitude 5° 58.22' W). Espartel Sill and Camarinal Sill are indicated by the acronyms ES and CS, respectively. The inset shows the model grid (decimated by a factor of two for the sake of clarity) with highlighted in red the section where the outflow has been computed.

In 2011, after a couple of accidents suffered by the mooring line that we ascribed to fishing activity, the monitoring in ES was temporarily interrupted and the line was moved to the Camarinal Sill (CS hereinafter, see Figure 1) looking for the safer conditions provided by the abrupt topography of the seafloor in this place (experiment CS00 in Table A-1). In the meanwhile a fisher-proof, more robust structure was devised and, after around 7 months of measurements in CS, the mooring line was brought back to ES again. During the 10 years life span of the monitoring station the mean duration of each single experiment has been 4 months approximately, with a total of 27 experiments in ES and one in CS.

The mooring line is less than 20m tall, it is equipped with an up-looking Acoustic Doppler Current Profiler (ADCP) embedded in a subsurface buoy and a single-point currentmeter and a

conductivity/temperature (CT) sensor, both clamped along the line below the buoy. An anchor of 1 ton approximately keeps the line on position and an acoustic release and two ARGOS beacons attached to the buoy complete the line. The scheme of the mooring line has changed little: from 2004 to 2006 the single-point currentmeter was an AANDERAA RCM9 Doppler instrument. After 2006 it was replaced by a Nortek Aquadopp Doppler. A 75 kHz Teledyne RDI ADCP has been usually employed, although in three experiments during years 2006-07 a 150 kHz model of the same manufacturer had to be installed instead of the lower frequency model for technical reasons. In these three experiments the current profile has higher vertical resolution but less coverage of the upper water column. Table A-1 displays information and the main features of all experiments.

Most of the times the ADCP was configured with a narrow bandwidth (WB1), in order to extend the profiler range [*Teledyne RD Instruments*, 2013a], and a number of pings per ensemble ranging from 40 to 50, with the exception of the first experiments and those accomplished by the 150 KHz model, which were configured with lower and higher number of pings, respectively. The ensemble interval was 30 minutes, while the bin width was set to 8 meters. In a few cases (asterisks in Table A-1) the single-point currentmeter failed to collect data.

3 Ancillary data

3.1 Numerical model

The two hindcasts of the MITgcm numerical model used in *Sammartino et al.* [2014] and [*Sánchez Garrido et al.* [2013]; 2014] have been exploited to help defining the interface (Section 6) and to depict and assess the cross-strait structure of the outflow (Section 7.3). The hindcasts cover the periods March 12 – June 23 and September 1 – November 29, 2011 and are referred as H1 and H2, respectively. As these hindcasts coincide with the gap of the series of 2011, a third hindcast of

shorter duration (March 18 to April 30, 2013, matching a fraction of the experiment ES23) has been included to validate the model against observations. This hindcast is referred as H3.

3.2 CTD/LADCP data

The cross section of ES has been routinely sampled since 2009 by means of Conductivity Temperature Depth (CDT) and Lowered ADCP (LADCP) casts. The LADCP is attached to the CTD structure to obtain simultaneous profiles of the thermohaline properties and the velocity field of the water column. The sampling consists of a series of 12-14 stations spanning across the strait with a mean inter-stations distance of ~2 km. A subset of 17 casts accomplished in the three deepest stations of the southern channel of ES from 2009 to 2014 (one of which coinciding with the moorings location), has been analyzed in Section 6 to help improving the characterization of the interface. This kind of observations, although more reliable than the modeled outputs, cannot be considered synoptic because of the high tidal variability observed in the area. Moreover, due to a series of logistic issues, the majority of LADCP casts was performed after the recovering of the moored line and during its maintenance onboard, and therefore they are not simultaneous with the ADCP record. For these reasons LADCP measures cannot replace the modeled outputs to estimate the cross-strait structure of the flow.

4 Data processing

4.1 Pre-processing

In order to obtain a reference depth of the ADCP head, which is necessary to derive the bins range, the pressure record of each experiment has been accurately checked. In those cases where a notable variation of the pressure was detected, a moving average filter was applied to assign a new, corrected depth to the sample. In the other cases where a small correction was necessary, a linear regression

155 worked adequately. The global drift for each experiment is rather negligible (see Table A-1). The
156 range of the first bin has been calculated as $R_{\#1} = B + 0.5 \cdot (W + X + L)$, where B is the blanking
157 distance, X the transmit pulse length, L the distance between sound pulses and W the bin thickness
158 [*Teledyne RD Instruments*, 2011]. The range of the rest of bins has been derived from the first one.
159 The bins affected by the sidelobe interference of the sea surface have been identified as those falling
160 within the distance from the surface given by $D = D_{ADCP} \cdot (1 - cos\theta) + W$, where D_{ADCP} is the
161 ADCP depth and θ is the angle of the instrument transducers [*Plimpton et al.*, 2004]. They have
162 been removed from the ADCP profile. The final number of effective bins considered in the present
163 study is reported in Table A-1.

164 **4.2 Attitude accuracy**

165 The ADCP measures velocities along the transducers axes and transforms them into east-north-up
166 (ENU) components. The operation requires information on the relative orientation of the ADCP head
167 with respect to the Earth's magnetic field (attitude), and the performance of the transformation
168 depends on the accuracy of this measurement. The effect of the local magnetic declination and the
169 accuracy of the ADCP tilt have been evaluated by following the procedure: (1) backward
170 transformation of the ENU components to the ADCP head reference (XYZ coordinates), (2)
171 application of the correction factor, either magnetic declination or tilt error, (3) forward
172 transformation of the XYZ components to the ENU reference (see *Teledyne RD Instruments* [2010]
173 for details on the rotation matrices employed in the transformations). The magnetic declination
174 decreased from ∼-3° in 2004 to ∼-2° in 2015 and accounts for a maximum variability of the along-
175 strait current of approximately ±3 cm s^{-1}. Its effect has been corrected in the original profiles. It is
176 worth mentioning that the ADCP internal compass was calibrated ashore three times during the ten
177 years of measurements, in occasion of the change or loss of the ADCP/buoy compound, with the
178 instrument embedded as it was deployed (no compass calibration is suitable onboard). While it
179 compensates the effect of the buoy stainless steel frame, any further effect of the neighbor magnetic

180 field (the battery packs have been always degaussed prior to be installed) has been assumed
181 negligible. The effect of the tilt uncertainty (±1° as reported by *Teledyne RD Instruments* [2013b])
182 has been estimated in ±1 cm s^{-1} and no further correction has been applied. In the whole set of
183 experiments, the tilt never exceeded the safety limit established by the manufacturer of ±20°
184 [*Teledyne RD Instruments*, 2013b].

185 **4.3 Outliers removal**

186 Each ADCP profile is the result of averaging a number of single pings measurements over a given
187 time interval (ensemble). The averaging reduces the random error by a factor of $\sqrt{N}$, where N is the
188 number of averaged pings. While the theoretical error is known by *a priori* estimation of the
189 instrument performance based on the user configuration, the uncertainty associated with each single
190 measurement due to environmental sources is unknown. This uncertainty is estimated by the
191 following equation [*Teledyne RD Instruments*, 2011]:

$$\sigma_e = \frac{\sigma_p}{\sqrt{N}} \quad (1)$$

192 where σ_e and σ_p are the errors associated to the ensemble and the single ping, respectively, both
193 unknown, in this case. The available information is the theoretical error of the ensemble σ'_e, which
194 we use to retrieve an estimation of the single ping error $\sigma'_p = \sigma'_e \cdot \sqrt{N}$, and the effective number of
195 pings in the ensemble averaging, which is recorded in the ADCP file (percentage good #3, if the
196 coordinate system is ENU, see *Teledyne RD Instruments* [2013b]). By inverting equation (1), we
197 obtain an estimate of the ensemble uncertainty:

$$\sigma_e^* = \sigma'_p \cdot \left(WP * (1 - PG_3/100)\right)^{-1/2} \quad (2)$$

198 where WP is the maximum number of pings used in the average (the number of pings per ensemble
199 set in the configuration file) and PG_3 is the percentage of pings that were excluded from the

ensemble average, which are those pings with more than one beam rejected. Equation (2) reduces to $\sigma_e^* = \sigma_p' \cdot (WP)^{-1/2} \equiv \sigma_e'$ if $PG_3 = 0$, and the estimated uncertainty of the ensemble equals the theoretical one ($WP \equiv N$).

A threshold of twice the standard deviation of the distribution of σ_e^* was applied to remove all the ensembles with uncertainty exceeding this value and, in case of more than 50% of the samples failing this test, the whole bin was deleted. Figure 2a shows a fragment of the experiment ES02 as an example of the performance of this procedure.

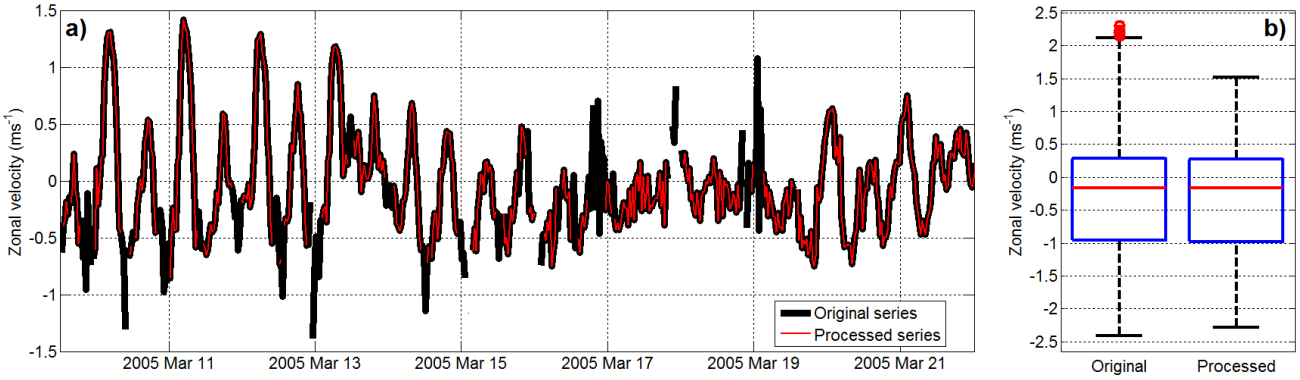

Figure 2 – (a) Zonal component of the velocity at bin #36 (46 meters depth) during part of the experiment ES02 displaying the original and the processed series. The high frequency oscillations around the local minima in the first half of the series and some suspicious high frequency events during the second half have been effectively removed. (b) Distribution of the original and processed series of the whole experiment showing the centrality (median, red line) and dispersion (thickness of the blue box), which are almost entirely preserved during the process. The outliers (dots outside the box) are effectively removed.

As last step of the data processing scheme, the profiles have been interpolated vertically, from 330 to 20 meters depth, with an interval of 2 meters, in order to obtain a common reference for all experiments.

5 Boundary layer current

The blanking distance of the ADCP and the length of the emitted pulse, both determining the distance from the instrument transducers to the first measured bin, along with the fact that the instrument is about 20 m above the seafloor, locate the first effective bin at approximately 30-40

meters above the bottom. Therefore, the extrapolation of the velocity profile in the near-bottom layer is a relevant issue to compute the outflow.

5.1 Mean profile

Figure 3a shows the box-whisker plot of the zonal velocity recorded during the ES12 experiment as an illustration of the typical baroclinic exchange at the western exit of the SoG. The interface is located at approximately 190 meters, separating the upper eastward inflow of rather constant mean velocity (25 cm s^{-1}) by the lower westward outflow with a maximum mean velocity of ~1.3 m s^{-1} at ~280 m. The length of the whiskers (dashed segments) is constant in the vertical with a slight widening just below the interface, while the vertical distribution of the outliers (circles) reveals the zones with more variability. These outliers around the interface reflect the periodic inversion of the current at these depths. Actually they give a hint on the thickness of the interfacial layer: approximately 50 meters, in agreement with the results by *García Lafuente et al.* [2013]. On the other hand, the concentration of outliers between 250 and 300 meters depth is the signature of the very weak westward current, or even eastward current, reaching the lower layer during the ebb flow of spring tides.

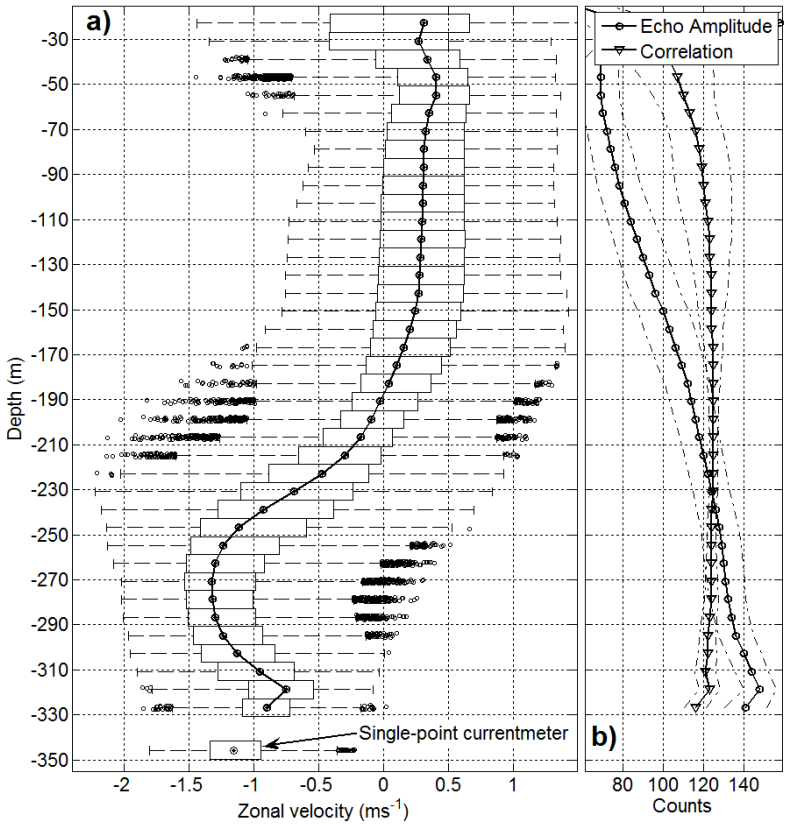

Figure 3 – (a) Box-whisker plot of the zonal component of the velocity measured by the ADCP and the single-point currentmeter in experiment ES12. (b) Vertical profile of the mean ADCP echo amplitude and correlation (see legend) with their respective standard deviation (1σ) limits (dash-dotted line).

The deepest bin of the ADCP lies out of the expected position for a logarithmic profile that vanishes at the seafloor. The effect of the ADCP ringing (the noise introduced by the resonance of the ADCP housing affecting the first bin measurement) emerges as the most intuitive explanation, which is further confirmed by the otherwise unexplained diminution of the correlation and echo amplitude in the first bin (Figure 3b). On the other hand, the velocity measured by the single-point currentmeter seems to be fairly coherent with the first bin, although it suggests an unrealistically high bottom boundary velocity. The puzzling question is that such structure is found in almost all the experiments with different ADCPs and varying mooring line schemes, a fact hardly explainable.

5.2 Single-point currentmeter measurements

In the first six experiments an AANDERAA RCM9 Doppler currentmeter was employed: the instruments measures amplitude and direction of the horizontal velocity but it does not give

information on the attitude and the accuracy of the measure. According to the manufacturer specifications [*Aanderaa Instruments*, 2002], the theoretical error is $O(10)$ cm s^{-1}. In the rest of the experiments the line was equipped with a NORTEK AQUADOPP Doppler currentmeter that measures the three-dimensional velocity field and the attitude of the instrument. Its declared accuracy is 1.5 cm s^{-1} and it offers a special acquisition mode called *diagnostic*, which performs an online evaluation of the uncertainty of the measurement. We exploited this mode to obtain an estimate of the ensemble uncertainty, which amounts to roughly four times the expected theoretical value. The discrepancy can be explained by the vibration of the mooring line and the turbulence induced by the instrument clamp. The uncertainty of the observations of the single-point currentmeter is higher than the one of the rest of the profile (column 6 of Table A-1), and then they must be considered more cautiously.

5.3 Mean velocity profile in the bottom boundary

As we are interested in the exchanged flows, the East-North Cartesian velocity has been rotated 17° anticlockwise, which is the angle of the axis of the SoG with respect to the East [*Baschek et al.*, 2001; *Sánchez Román et al.*, 2008]. The along-strait component is the only one considered hereinafter.

The profile showed in Figure 3a suggests the presence of a frictional layer in which the horizontal velocity vanishes logarithmically. The way in which the profile is extrapolated in this layer depends on the relative importance of rotational and nonlinear terms, which is assessed by the Rossby number $Ro = U/fL$, with U and L the horizontal velocity and length scale of the flow, respectively, and f the Coriolis parameter. In the SoG, U is $O(1$ m $s^{-1})$, f is $O(10^{-4}$ $s^{-1})$, and L is $O(10^{4}$ m), such that the Rossby number is $O(1)$. Therefore, the nonlinear and rotational terms are comparable [*Bormans and Garrett*, 1989; *Sánchez Garrido et al.*, 2011].

In case of predominance of the rotational term, the velocity profile would be modeled according to the Ekman bottom layer theory. The solution for the along-strait component of the velocity u_E in the frictional layer is (see *Pond and Pickard* [1983] for instance):

$$u_E = u_o \cdot \left[1 - e^{-\pi z/D_E} \cdot \cos(\pi z/D_E)\right] \quad (3)$$

where u_o is the interior velocity (above the frictional layer), z the distance from the bottom and $D_E = \pi \cdot (2A_z/|f|)^{-1/2}$ the thickness of the layer, A_z being the vertical eddy viscosity coefficient. The theory assumes a barotropic velocity out of the bottom layer. However the current in ES is markedly baroclinic. Equation (3) was slightly modified therefore to take into account the discrepancy between the maximum velocity of the lower layer and the theoretical barotropic velocity in the formula:

$$u_E = \frac{u_o \cdot \left[1 - e^{-\pi z/D_E} \cdot \cos(\pi z/D_E)\right]}{1 - \left(u_E\left(z_{u_{max}}\right) - u_{max}\right)} \quad (4)$$

where $u_E\left(z_{u_{max}}\right) = u_o \cdot \left[1 - e^{-\pi z_{u_{max}}/D_E} \cdot \cos\left(\pi z_{u_{max}}/D_E\right)\right]$ is the Ekman velocity at the depth $z_{u_{max}}$ of the maximum velocity. Equation (4) can be rewritten as:

$$u_E = \frac{u_o \cdot \left[1 - e^{-\pi z/D_E} \cdot \cos(\pi z/D_E)\right]}{1 + u_o \cdot e^{-\pi z_{u_{max}}/D_E} \cdot \cos\left(\pi z_{u_{max}}/D_E\right)} \quad (5)$$

Equation (5) was least square fitted to the deepest portion of the vertical profile, from the maximum velocity to the second ADCP bin (the first one is excluded), assuming a zero velocity at the seafloor. Figure 4 shows the good agreement of the Ekman model fit with the ADCP data, although it reproduces badly the values of the first bin and the single-point currentmeter.

A second choice to model the velocity profile is the *law of the wall* (LoW hereinafter), valid for irrotational turbulent flows where the inertial forces dominate (see *Thorpe* [2007] for instance). The prescribed velocity u_W has the solution [*Kundu and Cohen*, 2004]:

$$u_W = \frac{u^*}{k} \cdot \ln\left(\frac{z}{z_0}\right) \quad \textbf{(6)}$$

Here k is the von Karman's constant, estimated experimentally as 0.41, and z_0 is the height above the bottom where the velocity is zero, which is known as the apparent *roughness length*. The term u^* is known as the *friction velocity*, a function of the shear stress T_x at the bottom: $u^* = \sqrt{T_x/\rho}$, with ρ the density of water. In a turbulent flow it can be expressed in terms of the vertical eddy viscosity: $u^* = \sqrt{A_z\, \partial u/\partial z}$ [*Stewart*, 2009], in which case equation (6) can be rewritten as:

$$u_W = \frac{1}{k} \cdot \sqrt{A_z \frac{\partial u}{\partial z}} \cdot \ln\left(\frac{z}{z_0}\right) \quad \textbf{(7)}$$

As for equation (5), equation (7) was least square fitted to the deepest portion of the vertical profile, with unknowns A_z and z_0. To carry out the fit, a first guess of u^* was derived using the A_z coefficient provided by the fit of the Ekman model and the velocity shear ($\partial u/\partial z$) computed using the maximum velocity and the velocity in the second bin, as in *Thorpe* [2007]. The mean friction velocity u^* of the whole set of experiments was 4 cm s^{-1}, in very good agreement with previous estimations [*Johnson et al.*, 1994; *Perlin et al.*, 2005], and the averaged roughness length z_0 was O(1 m), agreeing with the observed roughness of the seafloor too [*Izquierdo et al.*, 1996].

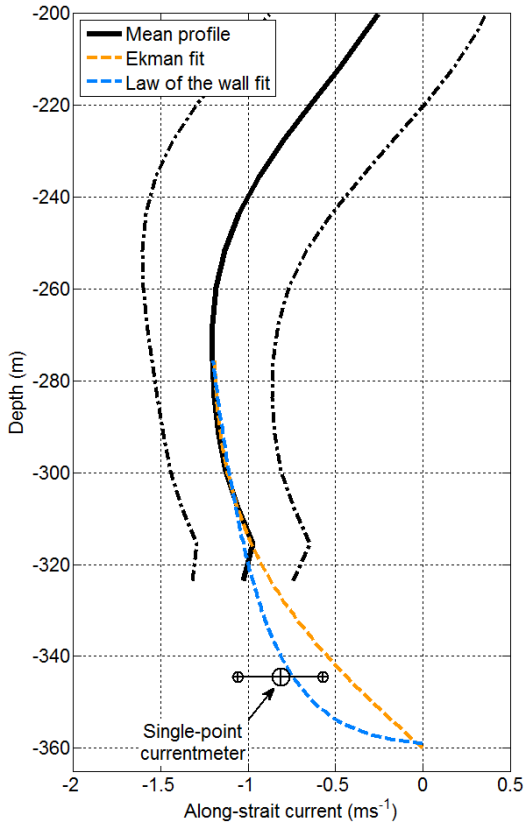

Figure 4 – Zoom of the deeper portion of the mean profile in experiment ES23, showing the velocity in the bottom boundary layer inferred from the least square fit of the modified Ekman (orange line) and the LoW (blue line) models. Dash-dotted lines indicate the ±1σ limits of the mean profile.

LoW performs better than the Ekman model with the observations (the first ADCP bin and the value of the single-point currentmeter), but it does slightly worse in the upper portion of the ADCP profile (Figure 4). *Kundu* [1976] concluded that the bottom boundary layer could be divided into two partially overlapped sub-layers, an outer region where the Coriolis force balances the frictional terms and an inner region where the velocity vanishes logarithmically and the rotational terms become negligible. According to the previous discussion and the results in Figure 4, this seems to be our case.

5.4 Instantaneous velocity profiles in the bottom boundary

Both models provide satisfactory results for the mean profile. However, the Ekman model is especially sensitive to the steadiness of the flow, which is a drawback for the instantaneous flows. Rotation is expected to be relevant at periods longer than f^{-1} [*Kundu*, 1976], whereas LoW has not

313 this limitation. With an original sampling interval of 30 min, the time series is strongly influenced by
314 tides, whose periodicity is less or of the same order as f^{-1}, a reason that explains why LoW
315 performs noticeably better than the Ekman approach with the instantaneous profiles. Nonetheless and
316 as we show next, the goodness of the fit with this law is rather variable and exhibits a marked
317 periodicity dominated by the diurnal frequency.

318 Figure 5a,b present the results of the harmonic analysis of the series acquired in the experiment ES01
319 for the main semidiurnal (M_2) and diurnal (K_1) constituents. Figure 5c shows that the variance
320 explained by tides decreases sharply near the bottom, where the turbulence generated by the
321 interaction of the outflow with the bathymetry becomes more important. It means that tides are not
322 the main source of variability in the layer where we are attempting to devise a reliable velocity
323 profile. Above this layer, the amplitudes (Figure 5a) show a similar depth-dependence with local
324 maxima in the upper and lower layer and a nearly constant amplitude ratio of ~4. In addition, M_2
325 presents a local minimum near the interface. Phases (Figure 5b) are also similar, with a rather
326 constant difference of ~50°, although a remarkable feature in the K_1 profile emerges: the sudden
327 phase shift of ~180° of the two deepest bins that are in phase opposition with respect to the rest of
328 the bins. This shift is accompanied by a local minimum of null amplitude at the same depth (Figure
329 5a), which strongly suggests a standing-wave pattern in the vertical for K_1 with a node at the depth of
330 the third bin. This pattern seems to be behind the deficient performance of LoW in some profiles, as
331 it is discussed next.

332 To further investigate this issue, the residuals between the lower part of the ADCP profile and its fit
333 by LoW were submitted to harmonic analysis. The main contribution to the residuals comes from K_1
334 constituent (29±2 cm s^{-1} amplitude), which is more than 50% greater than M_2 contribution (18±3 cm
335 s^{-1}), a fact further confirmed by the signal-to-noise ratio, which is one order of magnitude greater for

K_1. This ratio is two orders of magnitude greater for K_1 than for any other diurnal constituent as well, suggesting that K_1 dominates the source of the diurnal residuals left by the LoW fitting.

An example that illustrates this result is presented in Figure 5d: the two profiles correspond to the outflow peak of two consecutive cycles (see inset). In the profile labeled "A" the K_1 contribution is scarce and the observed regular profile is basically due to the semidiurnal constituents, M_2 in particular, which is at its maximum. In the next cycle, labeled "B", K_1 is at its maximum and adds to the semidiurnal peak except in the two or three deepest bins where the contribution is negative due to the ~180° phase shift. It distorts the lower part of the profile with regards to the much more regular previous peak, causing a deficient LoW fitting and, hence, a K_1 periodicity of the residuals (see also the animation in the supplementary material A in the online version of the paper).

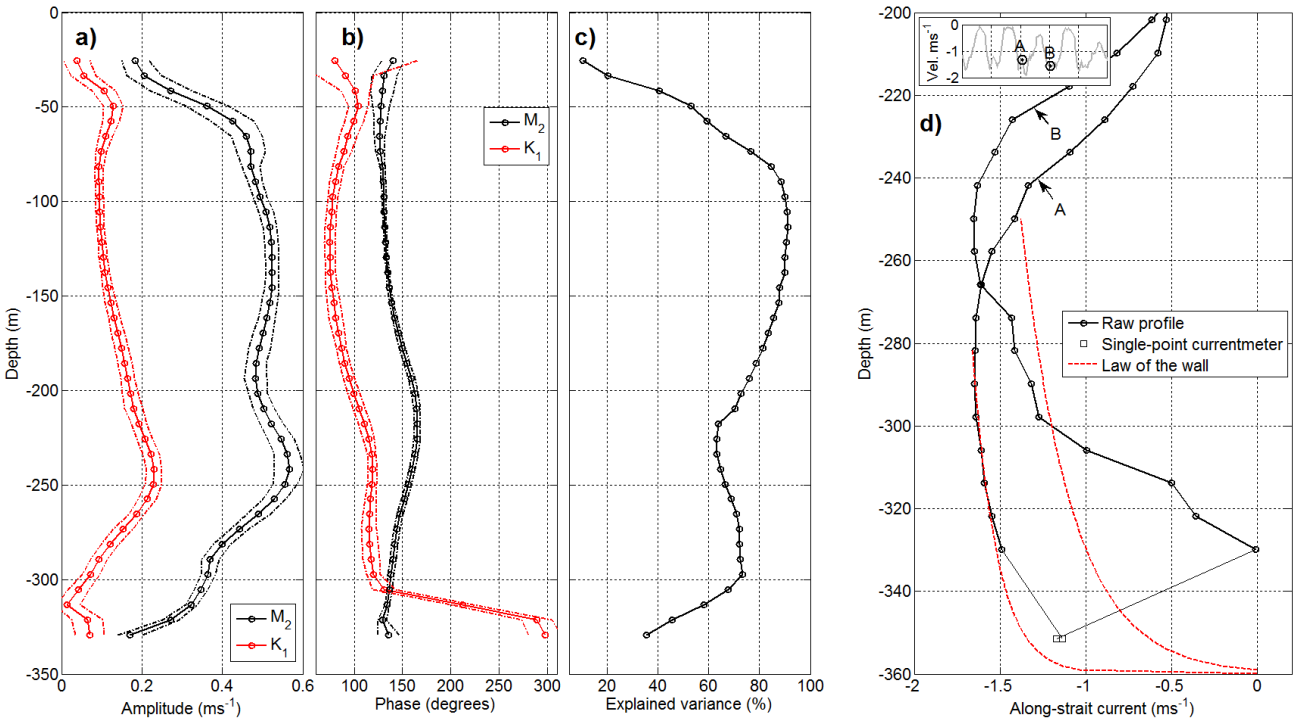

Figure 5 – (a) Vertical profiles of the amplitude of the along-strait component of the velocity for M_2 and K_1 constituents, deduced from the experiment ES01. Dash-dotted lines represent the errors associated to the analysis. (b) Same as in (a) except for the phase. (c) Variance explained by the harmonic fitting. (d) Vertical profiles of the along-strait velocity at the times indicated in the inset, which shows the along-strait velocity at 250m depth. LoW fitting for each profile is also plotted (see legend). Notice the different vertical scales in panels (a), (b) and (c) with respect to panel (d).

This issue is quite surprising and may deserve further investigation, although it is out of the scope of the present work. Anyhow, the effect of the periodic fail of the LoW on the long-term computation

of the outflow is negligible, and the following empirical solution is proposed to infer the bottom layer current of the whole series: LoW is fitted to all profiles (single-point currentmeter included) and the mean value of the RMS residuals is computed. Whenever a given extrapolation provides a RMS residual lower than the mean value, the obtained LoW profile is kept. Otherwise, the profile is replaced by a linear interpolation between the first bin of the ADCP and the bottom, where a null velocity is assumed (see also the animation in the supplementary material A in the online version of the paper).

6 Interface

6.1 Different choices of a suitable interface

The best variable to define the interface between AW and MW waters is the salinity, as it is the property mainly weighing the density gradient [*Bray et al.*, 1995]. In the literature, the reference isohaline has been defined either directly by estimating the outflow salinity transport [*Bryden et al.*, 1994] or as the isohaline that maximizes the outflow [*García Lafuente et al.*, 2000; *Naranjo et al.*, 2014]. This last choice, when both velocity and salinity are available, solves the dual aim of defining the isohaline in a non-arbitrary way and providing a reliable tracking of the position of the zero-crossing velocity depth (strictly related with the former) even when it is not defined at tidal frequency (see next paragraphs). The maximized outflow we are interested in, accounts for the bulk of MW naturally flowing westwards and the portion of AW partially mixed with MW and entrained back to the Atlantic Ocean [*García Lafuente et al.*, 2000; 2013]. This proxy is coherent with the evolution of the outflow along the main axis of the SoG (specially from CS westwards) that undergoes an increase of size and a freshening from east to west [*Bray et al.*, 1995]. The interface based on the isohaline that maximizes the outflow will be used later with modeled outputs (Section 7.3).

In our experimental study, however, this proxy is not suitable because of the lack of salinity observations along the water column, so that the interface has to be inferred from the velocity observations exclusively. In order to assess this inference, both modeled and observed (LADCP/CTD) profiles have been previously analyzed. Figure 6a shows the mean salinity and the along-strait velocity profiles simulated by the model at the grid point coinciding with the ES station. The isohaline that maximizes the outflow is S=36.66, in good agreement with *Naranjo et al.* [2014], and its depth, D_{S_m}, matches the depth of the zero crossing, D_{V_0}, fairly well.

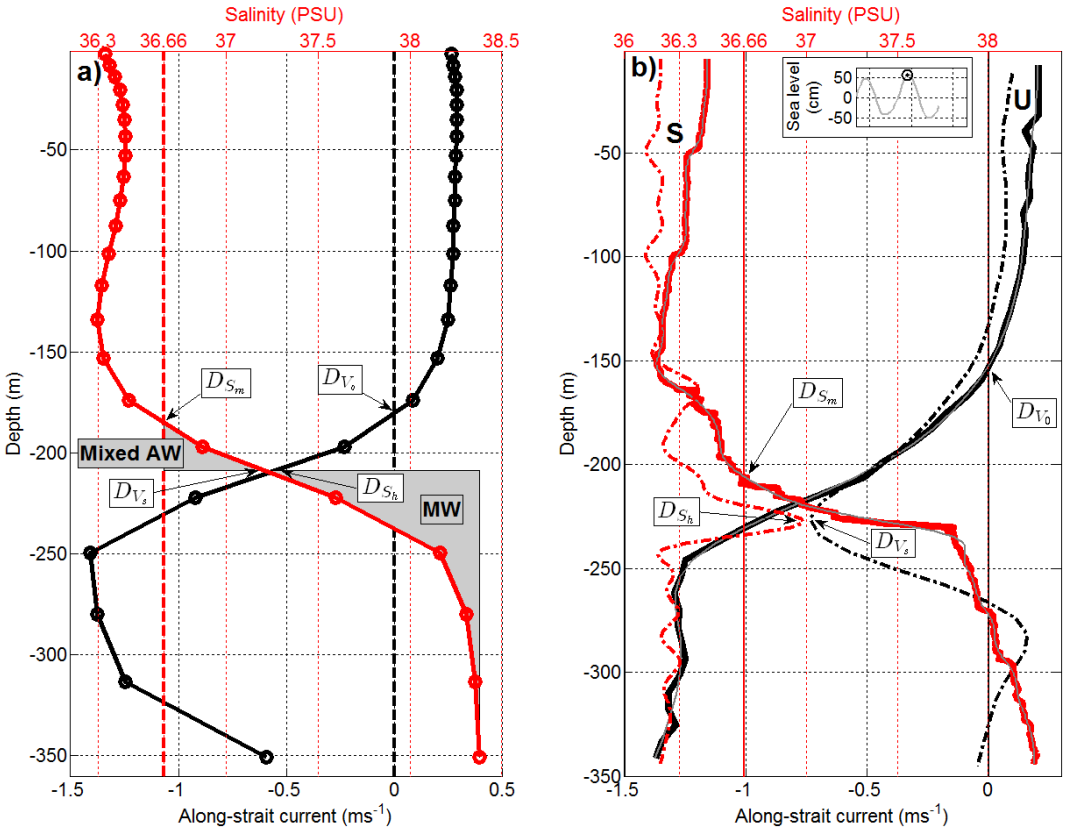

Figure 6 – (a) Mean along-strait velocity and salinity simulated by the model at the mooring location. The gray-shaded areas indicate the portion of MW and mixed AW involved in the outflow. (b) An example of a CTD/LADCP cast in the mooring location on 22nd of November 2011. The thick lines represent the original profiles of salinity (red) and along-strait velocity (black), the thin gray lines are their smoothed profiles obtained by applying a low-pass Butterworth filter with pass and stop band frequencies of 15^{-1} and 10^{-1} m^{-1}, respectively. The dashed-dotted lines indicate the first derivative of the smoothed profiles, which are plotted to highlight the coincidence of the depth of the extremes. They have been arbitrarily scaled and shifted along the x-axis for the sake of clearness. The inset shows the sea level in Tarifa Port. The zero-cross velocity (D_{V_0}), the depth of the isohaline that maximizes the outflow (D_{S_m}), the maximum velocity shear (D_{V_s}) and the maximum salinity gradient (D_{S_h}) are indicated in both graphs.

The depth of zero velocity, D_{V_0}, lies above the depth of the maximum salinity gradient, D_{S_h}, which would correspond to the depth above (below) which the water presents prevailing Atlantic (Mediterranean) characteristics. As D_{V_0} is shallower than D_{S_h}, the outflow at ES comprises a portion

382 of the water column with prevailing Atlantic characteristics, approximately the layer between D_{S_h}
383 and D_{S_m} (gray areas in Figure 6a), which is entrained by the swift westward outflow of purer
384 Mediterranean water, as discussed in *García Lafuente et al.* [2013].

385 In a hypothetical steady state, inflow and outflow would be separated by the D_{V_0} surface, which
386 would be always defined. In such a high energetic system as the SoG, however, that is not the case.
387 External forces acting at subinertial frequency, such as atmospheric pressure gradients or wind stress,
388 induce interface fluctuations of a few tens of meters [*García Lafuente et al.*, 2002], while, more
389 drastically, the barotropic tidal flow periodically breaks the baroclinic structure of the flow reversing
390 the inflow with semidiurnal periodicity [*García Lafuente et al.*, 2011; 2013]. Under these
391 circumstances D_{V_0} does not exist and the upper bound of the outflow has to be re-defined. Figure 6b
392 helps to understand what is meant. It shows a CTD/LADCP cast in the location of the mooring,
393 performed during the slack tide corresponding to high water, extracted from the series of analyzed
394 casts, as an example of the vertical distribution of the interfaces discussed (the other casts are
395 equivalent examples and are not shown). The previous strong westward flow had lifted the
396 instantaneous D_{V_0} with respect to its mean position and, at that moment, it is approximately 50
397 meters above D_{S_m}. The fraction of the water column between D_{V_0} and D_{S_m} is occupied by water with
398 AW salinity, which has been swept westward prior to be mixed with MW. Choosing D_{V_0} as the upper
399 bound of the outflow will result in a noticeable overestimation of the outflow that now would include
400 a portion of AW that should not be considered. The approach devised to work out the interface must
401 be able to follow D_{V_0} whenever it represents a reliable proxy of the interface, and infer a new
402 interface when D_{V_0} does not exist or its existence implies an unrealistically high westward transport
403 of unmixed or poorly mixed AW.

6.2 Interface computation

An alternative, firstly proposed by *Tsimplis and Bryden* [2000] and adopted by [*Sánchez Román et al.* [2009]; 2012], is to use the depth of maximum vertical shear of the horizontal velocity, (D_{V_s} in Figure 6), which is always determined, even in the instantaneous profiles. Figure 6 shows that D_{V_s} at ES is generally deeper than D_{V_0}, while it matches D_{S_h} very well, which is an expected result taking into account the role of the halocline in the generation of the velocity shear [*Bray et al.*, 1995]. However, should D_{V_s} be used as the interface, it would provide an underestimation of the outflow because the above referred portion of water column with prevailing AW characteristics entrained by the deeper outflow (the gray-shaded area on the left of Figure 6a), would not be considered (the animation B in the supplementary material illustrates the behavior of D_{V_0} and D_{V_s} and helps to understand the differences between both variables, which sometimes is quite drastic).

To avoid this underestimation, D_{V_s} must be lifted by a certain quantity. *Sánchez Román et al.* [2009] used a fixed value, based on the averaging of the distance between D_{V_0} and D_{V_s}, estimated at sub-tidal time scale. Here a slight more sophisticate approach is proposed: for each experiment, the distance $\Delta_D = D_{V_0} - D_{V_s}$ is computed for every profile whenever possible, that is, whenever D_{V_0} exists. As an example, Figure 7 shows the histogram of Δ_D for the experiment ES03. It suggests a bimodal distribution with uneven distribution of probability (with a ratio of approximately 3:1). The large tail on the right corresponds to the samples when D_{V_0} rises and separates from D_{V_s} more than usual, involving unmixed or scarcely mixed AW that should not be included in the computation of the outflow (this situation is usually met during the flood tide). Therefore, the effective distance (Δ'_D) by which D_{V_s} will be raised to obtain a realistic interface at ES, must be computed excluding this tail.

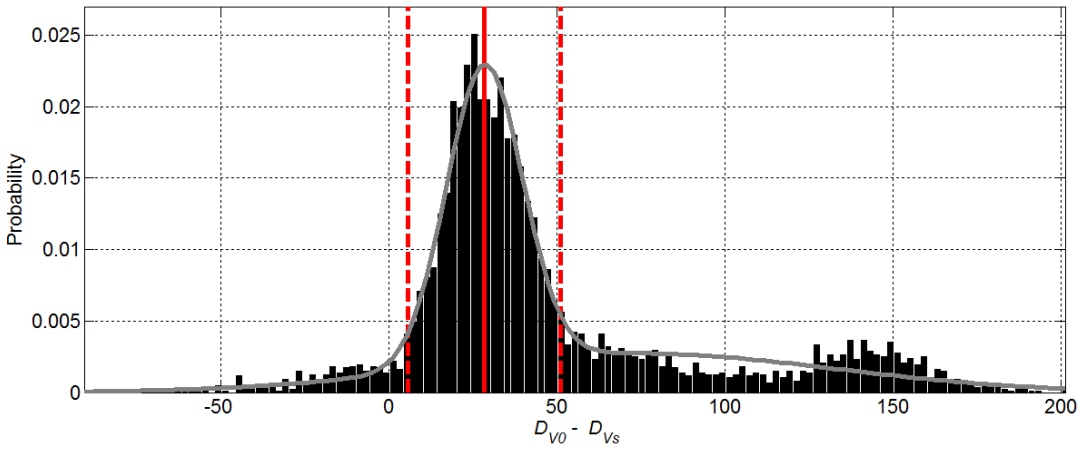

425

426 **Figure 7 – Probability histogram of the distance D_{V_0} - D_{V_s} for experiment ES03. The superposed gray line is the fit made with two Gaussian**
427 **PDFs. The vertical red lines display the mean of the first Gaussian (solid) and its 2σ interval (dashed).**

428 To this end, the histogram is fitted by a mixture of two Gaussian PDFs and only the fraction
429 comprised between the mean plus/minus twice the standard deviation of the distribution with lower
430 mean is retained (the area comprised between the two dashed lines in Figure 7). This subset of Δ_D
431 presents a number of temporal gaps corresponding to the times D_{V_0} is not defined. These gaps are
432 filled using harmonic analysis to finally obtain the desired series Δ'_D. The interface D_{V_s} is then lifted
433 by Δ'_D to obtain the series $D'_{V_0} = D_{V_s} + \Delta'_D$, which we consider the most reliable interface depth to
434 carry out the outflow computations.

435

436 # 7 Outflow computation

437 ## 7.1 The southern channel

438 The ES station is deployed in the main channel of the section, which is located close to the Morocco
439 coast and the south of Majuan bank (Figure 1). Not only the bulk of the outflow moves along this
440 channel but also, and from a practical point of view, this is the only place where observations are
441 available. Therefore, an estimation of the outflow across the southern channel is carried out first,
442 assuming the single velocity profile as representative of this portion of the section. The effect of this
443 assumption will be assessed in Section 7.3.

444 The instantaneous outflow is defined as:

$$Q(t) = \int_{bottom}^{D'_{V_0}(t)} u(t,z)A(z)dz \quad \textbf{(8)}$$

445 where $u(t,z)$ is the instantaneous along-strait velocity at depth z, and $A(z) = w(z) \cdot h_{bin}$ is the area
446 slice at depth z, with $w(z)$ the width of the channel (the southern channel in this case) at this depth
447 and h_{bin}=2m the resolution of the interpolated velocity profile (Section 4.3). The upper limit of the
448 integral is the interface depth D'_{V_0} computed in the previous section.

449 An interesting question regarding the flow computations is to estimate the contribution of the tidal
450 variability to the long-term exchange, the so-called eddy fluxes. Let us consider a slowly-varying
451 component of the outflow, Q_S, characterized by the sub-tidal variability of the velocity. As a product
452 of the velocity by the layer thickness (aside the channel width that is constant), Q_S depends directly
453 on the subinertial velocity and indirectly on the interface D_{V_0} computed on the same velocity. We
454 define the operator $\langle ... \rangle$ as a low-pass 8-th order Butterworth filter (with pass and stop band
455 frequencies of 38^{-1} and 28^{-1} h^{-1}, respectively, to remove tidal oscillations) and we compute the
456 filtered velocity $\langle u(t,z) \rangle$ and the corresponding zero-crossing interface $D_{\langle V_0 \rangle}(t)$. Q_S is defined as

$$Q_S(t) = \int_{bottom}^{D_{\langle V_0 \rangle}(t)} \langle u(t,z) \rangle A(z)dz \quad \textbf{(9)}$$

457 and coincides with the outflow in absence of tides. Notice that $D_{\langle V_0 \rangle}$ is always defined for the
458 velocity series $\langle u(t,z) \rangle$, and represents the upper limit of the integral in equation (9).

459 On the other hand, we can apply the same filtering operator to the outflow $Q(t)$ to calculate the sub-
460 tidal outflow $\langle Q(t) \rangle$. The difference between $\langle Q(t) \rangle$ and $Q_S(t)$ will be not null if there is a positive
461 correlation between the tidal oscillations of the velocity and the interface. This difference is the eddy
462 fluxes contribution, where the term eddy is inherited from the study of the covariance of the high

frequency anomalies of wind velocity and substance concentration in air, used in Atmospheric Science [*Foken et al.*, 2012]. The eddy fluxes have been shown to be very important in other sections of the SoG, mainly in the principal sill of CS [*Bryden et al.*, 1994].

The mean values of $\langle Q(t) \rangle$ and $Q_S(t)$ during the whole monitored period are -0.82 ± 0.16 Sv and -0.78 ± 0.15 Sv, respectively, revealing a mean contribution of the eddy fluxes $Q_E(t) = \langle Q(t) - Q_S(t) \rangle$ of 0.04 ± 0.03 Sv, approximately the 5% of the subinertial outflow. This percentage agrees well with the results presented in *Sánchez Román et al.* [2009]. Despite this low percentage, they can contribute by a larger percentage during spring tides as they exhibit a clear fortnightly modulation (spring-neap tidal cycles). The fortnightly and monthly constituents of $Q_E(t)$ prevail over the rest of the frequencies, and have amplitudes of 0.028 Sv and 0.017 Sv, respectively, explaining the 58% of the variance of the series. **¡Error! No se encuentra el origen de la referencia.**a shows the subinertial outflow $\langle Q(t) \rangle$ calculated for the whole set of experiments, while in **¡Error! No se encuentra el origen de la referencia.**b, a fragment of the series illustrates the contribution of the eddy fluxes and its modulation at fortnightly periodicity. The phase of M_{sf} is ~215 degrees, meaning that the maximum subinertial contribution of the eddy fluxes occurs approximately 1.4 days after the spring tide, in agreement with the age of the tide (a concept first coined by *Garrett and Munk* [1971]) in the SoG.

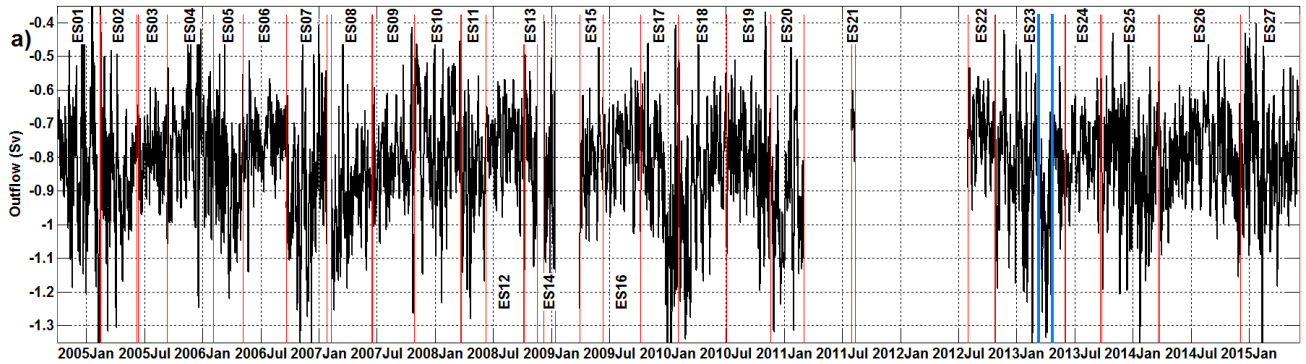

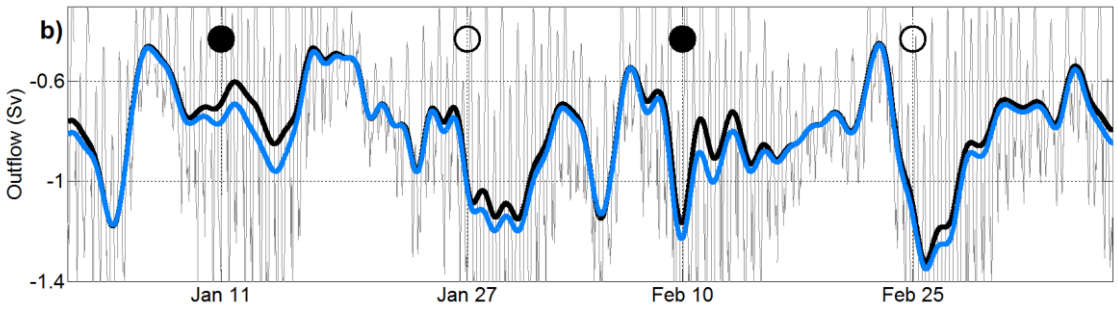

Figure 8 – a): Time series of the subinertial outflow $\langle Q \rangle$. The duration of each experiment is indicated by the vertical red lines. The blue segments indicate the fraction of the experiment ES23 used for the H3 hindcast validation (Section 6). b): a fragment of the series with the outflows Q (thin gray line), Q_S (thick black line) and $\langle Q \rangle$ (thick blue thick line). The difference between the blue and black lines is the eddy fluxes $Q_E(t) = \langle Q(t) \rangle - Q_S(t)$, which are more visible during new and full moon periods (empty and filled circles, respectively). The dates refer to year 2013.

An interesting issue illustrated in **¡Error! No se encuentra el origen de la referencia.**b is the much higher variability of the instantaneous outflow, $Q(t)$ with respect to the subinertial series $Q_S(t)$ (gray versus black lines in **¡Error! No se encuentra el origen de la referencia.**b). Actually $Q(t)$ shows a 1σ interval of 0.39 Sv, with the 5th and 95th percentiles of -0.22 and -1.47 Sv, respectively, and sporadic peaks exceeding -2.5 Sv. This confirms that the instantaneous transports are fully dominated by the tidal variability. To give some figures to this variability, the M_2 (S_2) amplitude and phase of $Q(t)$ are 0.38 (0.15) Sv and 154 (185) degrees, in agreement with *Sánchez Román et al.* [2012]. Similarly, the M_2 (S_2) amplitude and phase of the interface depth D'_{V_0} are 25 (10) meters and 351 (21) degrees.

7.2 Model validation

So far the outflow has been calculated by integrating the measured velocity over the southern channel of ES, and, as mentioned above, equations (8) and (9) implicitly assume that the time series collected at the point ES is valid for the whole section. The three hindcasts described in Section 3.1 are now used to investigate the cross-strait structure of the flow and assess the accuracy of this assumption.

The outputs of the H3 hindcast have been validated against the matching fraction of the experiment ES23 (see blue lines in **¡Error! No se encuentra el origen de la referencia.**b). Figure I, available in

497 the supplementary material in the online version of the paper, shows the mean profile and harmonic
498 analysis of both modeled and observed along-strait velocity. Mean currents (Figure Ia) are in a
499 highly satisfactory agreement, with the model showing a slightly higher amplitude in the
500 Mediterranean layer and slightly lower velocity in the bottom layer. Tidal M_2 amplitudes and phases
501 (Figure Ib,c) are also in good agreement, with some overestimation of the amplitude by the model
502 around the interface and a slight deepening of the phase peak, with respect to observations. Further
503 validations of the same model configuration over longer hindcasts, are extensively treated in
504 *Sammartino et al.* [2014] and *Sánchez Garrido et al.* [2014].

505 In order to make observations truly comparable with modeled outputs, the ADCP velocity profiles
506 have been integrated using the cross area defined in the model domain (LR), around 4% smaller than
507 the high resolution bathymetry provided by *Zitellini et al.* [2009] (HR), used so far. The resulting
508 outflow (second row in Table 2) is ∼6% lower than the one obtained by the same velocity profiles
509 applied to the higher resolution bathymetry (first row in Table 2). The observed outflow computed
510 on LR bathymetry can be now compared to the modeled outflow, where the modeled profile used in
511 the calculus is the one extracted at the grid point coinciding with the mooring position. The modeled
512 outflow is less than 2% weaker. This small difference is likely explained by the difference in the
513 interfaces depth (the model interface is meanly ∼6 meters deeper than the observations interface),
514 and the slightly higher velocity in the bottom layer provided by the observations, probably related to
515 the lower vertical resolution of the model with respect to the ADCP (39 meters versus 8 meters,
516 respectively, in the deepest cell).

517 **Table 2 – Mean outflow (Sv) computed to validate the H3 hindcast versus the overlapping fraction of experiment ES23. HR and LR stand for**
518 **outflow computations using the high and low resolution cross area based on the bathymetry provided by *Zitellini et al.* [2009] and the model**
519 **domain, respectively. Last row is the outflow computed from the model using a single velocity profile at the ES location and D'_{V_0} as interface.**

DATASET	Mean outflow (Sv)
OBS. ES23 (18mar-30apr) HR cross-area	-0.97
OBS. ES23 (18mar-30apr) LR cross-area	-0.91
MODEL, 1 point (D'_{V_0}) LR cross-area	-0.89

All these estimates are somewhat higher than the mean outflow computed in Section 7.1, an issue likely ascribable to the fact that the simulated period coincides with a strong anomaly of the subinertial outflow series (see blue lines in **¡Error! No se encuentra el origen de la referencia.**b), as well as the spring season, when the outflow peaks (Section 8).

7.3 Cross-strait structure

The evaluation of the cross-strait flow structure has been carried out using the numerical model outputs of the three hindcasts described in Section 3.1, where the criterion used to define the interface has been the isohaline that maximizes the outflow, D_{S_m}. This approach is even necessary in the northern part of the ES section where the currents are rather barotropic (see Figure 9) and the possibility exists that D_{V_s} is not always defined, especially at the shallower north of the section. The first row of Table 3 shows the outflow computed using D_{S_m} instead of D'_{V_0} and the single velocity profile of the hindcast H3 located at ES. Somehow, it repeats the computation showed in the last row of Table 2, but applying the salinity interface. Since, on average, D_{S_m} is ~10 m shallower than D'_{V_0}, the outflow is increased by 4% approximately (compare the first row of Table 3 with the last row of Table 2). It is worth mentioning that the different approaches to compute the outflow are of minor importance since we are looking for a ratio between the outflow across the whole section and across the southern channel: the difference between the ratios obtained using the two interfaces is less than 2% of the total outflow, where the advantage of using D_{S_m} with respect to D'_{V_0} is that the outflow is always computable with the former. This ratio whole section / southern channel will be subsequently applied to the observations across the southern channel in order to account for the fraction of the outflow flowing north of Majuan bank so far ignored.

At this point we also included the H1 and H2 hindcasts to obtain a more robust estimation based on longer simulations and, using all the model velocity data of the grid within the southern channel, we obtained a mean outflow of -0.72 ± 0.33 Sv. It reflects a reduction of the 23% with respect to the

single column estimation (first row of Table 3) in good agreement with *Sánchez Román et al.* [2009]. The reduction is due to the lateral friction that is neglected when the vertical velocity profile at a location is assumed valid for the whole (southern) channel. Finally, we computed the outflow across the whole ES section (northern and southern channels), which amounts to -0.97 Sv (third row of Table 3 and inset in Figure 9).

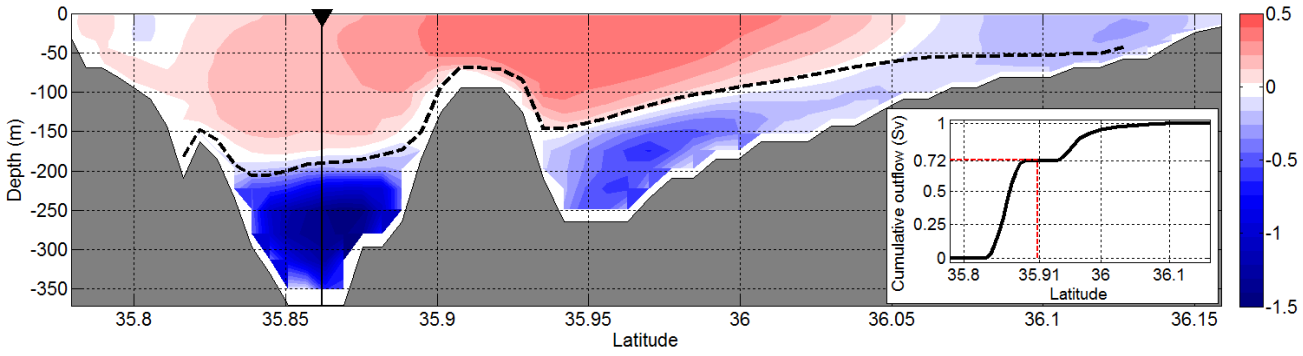

Figure 9 – Time average of the modeled along-strait velocity (m s^{-1}) during the H3 hindcast. The averaged D_{S_m} interface is shown in black dashed line and the mooring location is indicated by a black triangle. The inset shows the accumulated outflow across the whole ES section, the red dashed line indicates the Majuan bank and highlights the relative contribution of the southern and northern channels.

Summarizing, the outflow computed from a single profile of observations in the southern channel must be reduced by a factor of 0.77 (1-0.23) to correct for the overestimation coming from the neglect of the lateral friction. This result must be increased by a factor of 1.35 (1+0.35) to account for the so far ignored contribution across the northern channel. In other words,

$$Q'_{obs} = 1.35 \cdot (0.77 \cdot Q_{obs}) = 1.039 \cdot Q_{obs} \quad \textbf{(10)}$$

Therefore, the corrected mean value of the outflow based on observations would be -0.85 Sv.

Table 3 – Mean outflows (Sv) computed from modeled data. The first row shows the outflow across the southern channel computed using a single velocity profile at ES, which is assumed valid for the whole section. The second row is the same outflow recalculated using all the velocity data of the southern section grid. The third row is the same as the second one except for the whole ES section (north and south channels). The fourth row is the outflow derived from observations and the fifth row is the correction performed to take into account the drawbacks associated with the ADCP-based computations. See text for more details.

DATASET	Mean outflow (Sv)
MODEL H3, 1 point (D_{S_m})	-0.93
MODEL H1,H2,H3, all grid data, Southern channel (D_{S_m})	-0.72 (-23%)
MODEL H1,H2,H3, all grid data, Whole section (D_{S_m})	-0.97 (+35%)
OBSERVATIONS Southern channel (D'_{V_0})	-0.82

OBSERVATIONS Corrected (H1/H2)	-0.85

8 Mean outflow and time variability

The subinertial series of the Mediterranean outflow $\langle Q \rangle$ has been filtered by a moving average of 1-year length to assess the interannual variability of the series (Figure 10a) and obtain an estimate of the uncertainty associated with the accepted average of the outflow defined in the previous section. The 1σ interval of the moving average series is 0.03 Sv, which we accept as the searched uncertainty. Therefore, the best estimate of time-averaged outflow deduced from our dataset would be -0.85 ± 0.03 Sv. This uncertainty is in a reasonable agreement with *Boutov et al.* [2014]. A trend of -4.6×10^{-4} Sv year^{-1} has been also detected during the nearly 10-year life of the ES series, although it is not significant at the 95% confidence level.

Regarding the seasonal variability, the 1-month length moving average of the $\langle Q \rangle$ series (Figure 10a) gives a 1σ interval of 0.08 Sv, while the S_a annual constituent presents an amplitude of 0.06 ± 0.02 Sv and a phase of 240 ± 19 degrees. These results indicate that the annual signal is at least twice greater than interannual variability (measured in terms of the 1σ interval), and that the minimum (maximum) outflow occurs in early September (March).

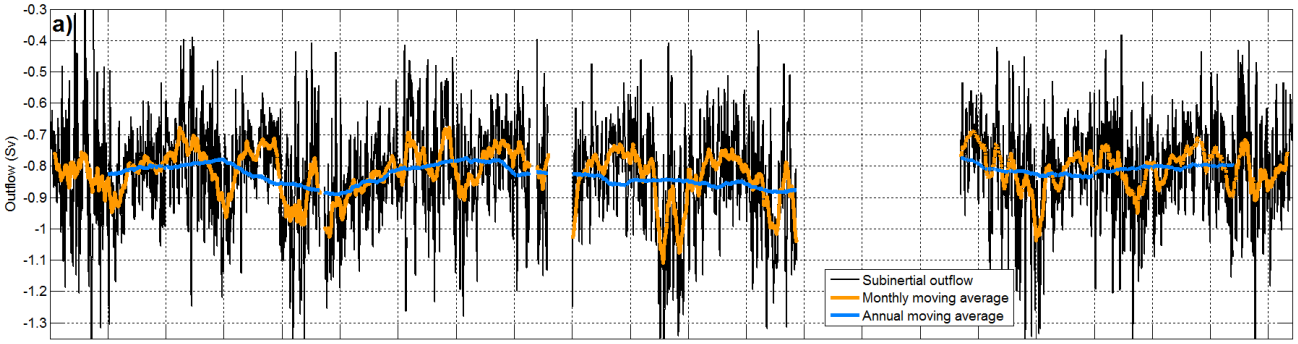

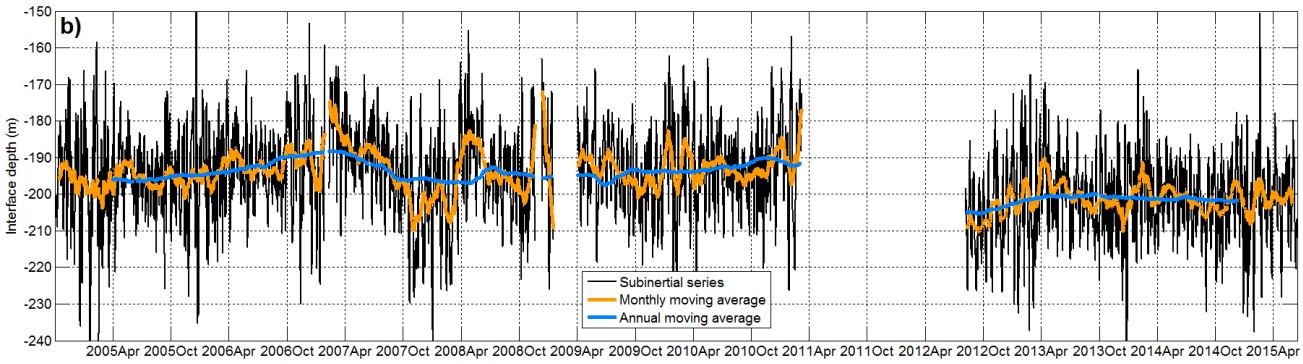

Figure 10 – Annual and monthly moving averages of the subinertial series of outflow (a) and interface (b).

The same treatment has been applied to the $\langle D'_{V_0} \rangle$ series (Figure 10b). The mean value is 195 ± 4 meters, the uncertainty being the 1σ intervals of the 1-year moving average. Notice that the interannual series of the interface depth is fairly specular with respect to the outflow (compare Figure 10a and b). Regarding the seasonal variability, the 1-month moving average provides a 1σ interval of ~6 meters, and the resulting series is not as much specular as the annual average with respect to its outflow counterpart. Actually, the S_a annual constituent of the interface has a phase of 115 ± 23 degrees, which means a phase difference of ~125 degrees with the outflow instead of the 180 degrees expected for the specular symmetry. The amplitude of the S_a constituent is 3.3 ± 1.5 meters, less than the 6 meters of the 1σ interval, which indicates the existence of other sources of variability for the annual scale.

The seasonal cycle of both outflow and interface depth is better appreciated in Figure 11 where the daily mean and 1σ interval computed for every year-day of all 10 year of available data are plotted (some kind of a ten-year climatological cycle). The series in Figure 11a (thick line) confirms the outflow peak in spring (April in this case) and minimum outflow in September. Not only the mean exhibits such a cycle but also the 1σ interval (gray area), suggesting more variability of the outflow in winter and less in summer. The spreading presents a peak of dispersion of ~0.11 Sv on year-day 60, roughly coinciding with the maximum of amplitude of the S_a constituent, and reduces to ~0.03 Sv in the summer. This variability comes from the higher meteorological variability of the winter months with respect to the summer season [*García Lafuente et al.*, 2002].

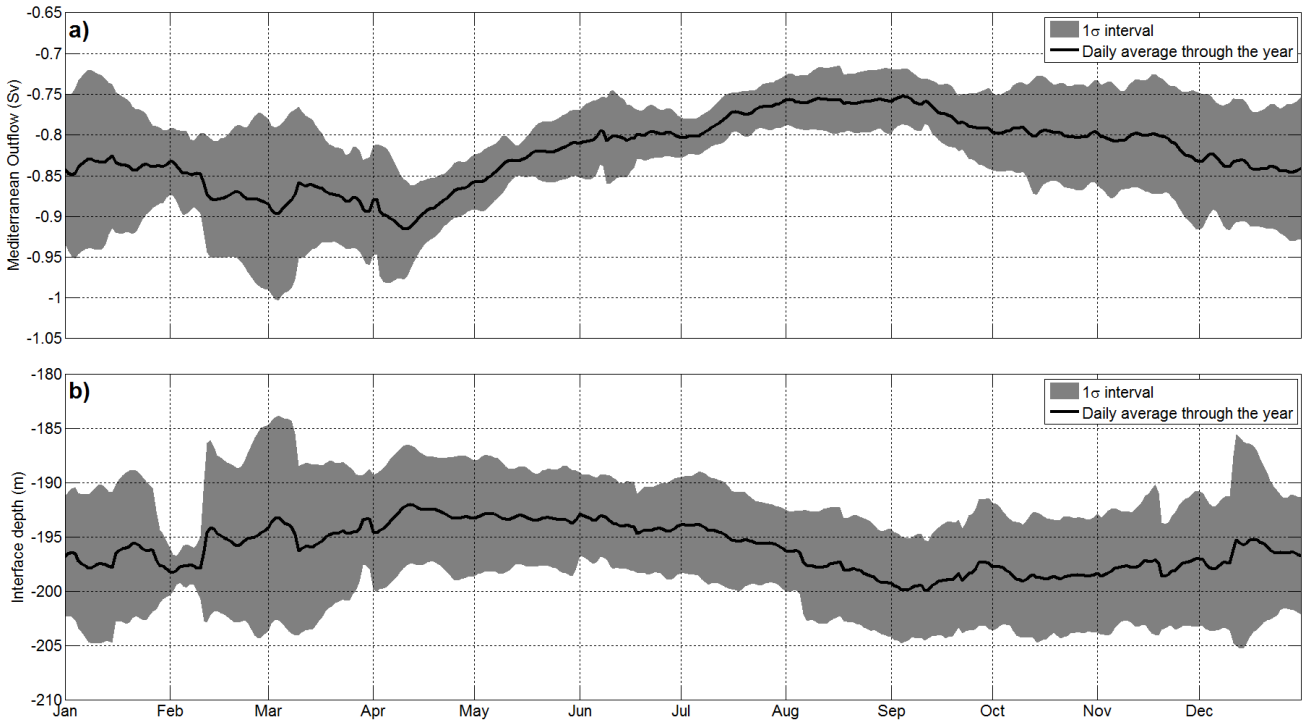

Figure 11 – Daily average of the 1-month moving average series, computed over all the years available of the series, for outflow series (a) and interface depth (b).

Figure 11b shows the corresponding results for the interface. It is shallower (deeper) when the outflow is maximum (minimum) in April (September), with a less pronounced phase lag between the two variables with respect to the results of the harmonic analysis. The $\langle D'_{V_0} \rangle$ daily means spread is still less pronounced in summer than in winter, although its seasonality is much lower than the outflow series.

9 Summary and Conclusions

A more than 10-year long series of ADCP observations at Espartel Sill in the western Strait of Gibraltar has been analyzed in this work in order to provide the most updated estimation of the outflow through the strait. After a careful check of the quality of the data and a detailed analysis of the extrapolation procedure to fill in the observational gap in the bottom layer, a time series of vertical profiles of the horizontal velocity every two meters, comprised from the bottom to 20m depth, was worked out. To compute the outflow, an upper bound of the lower layer (interface) is

610 required. To this aim, a method based on the depth of maximum vertical shear of the horizontal
611 velocity was devised, which provided a variable interface depth D'_{V_0}. Applying equation (8) with a
612 realistic bathymetry, we finally obtained an instantaneous time series of the outflow across the
613 southern channel of the ES section whose mean value is -0.82 Sv. Around 5% of it (-0.04 Sv) comes
614 from the eddy fluxes, a percentage much lower than in the main sill of Camarinal [*Bryden et al.*,
615 1994].

616 The estimate above has two important drawbacks that affect the computed time series. First, it
617 assumes that the single point velocity profile is valid throughout the southern channel section. In
618 other words, it ignores the lateral friction that damps out the velocity near the lateral boundaries, thus
619 causing an overestimation of the outflow. Second, it does not take into account the outflow occurring
620 north of Majuan bank, since this area cannot be sampled due to fishing activities. Obviously this
621 omission underestimates the total outflow in the previous computation. To address these issues, three
622 hindcasts of the MITgcm model, described and widely validated in *Sammartino et al.* [2014] and
623 [*Sánchez Garrido et al.* [2013]; 2014] have been employed to investigate the cross-strait structure of
624 the outflow and, hence, to produce correction factors to improve our first guess. The final result,
625 indicated in equation (10), is that our computation must be corrected by a factor of 1.039, very close
626 to 1, meaning that the overestimation caused by disregarding the lateral friction is nearly
627 compensated by the neglected outflow north of Majuan. Our best estimate of the outflow from the
628 ten-year time series is thus -0.85 Sv. It is in the upper range of the values based on observations
629 presented in Table 1 and modifies upward by ~8% the most recent ones by *Sánchez Román et al.*
630 [2009], *García Lafuente et al.* [2009] and *Soto Navarro et al.* [2010], who used shorter subset of the
631 same series and a similar approach for the estimation of the cross-strait structure.

632 The uncertainty of the value depends on the time-scale. The instantaneous outflow is dominated by
633 tidal fluctuations whose standard deviation is ± 0.39 Sv, although, sporadically, it can reach peaks

exceeding -2.5 Sv. A good choice for a representative variability at this time scale is the amplitude of M_2, 0.38 Sv, almost the same as the standard deviation. For longer periods, this interval is meaningless and the variability must be recalculated. After removing the effect of tides, the subinertial variability driven by meteorological variability has a standard deviation of ± 0.15 Sv, less than half the former value. For annual time scales, the meteorologically-driven fluctuations are averaged out and it is the seasonal cycle that prevails. Its variability is half the previous one (± 0.08 Sv) and agrees well with the 0.06 ± 0.02 Sv obtained for the Sa constituent in the harmonic analysis. At longer time scales, the interannual variability is further reduced to ± 0.03 Sv, which is the uncertainty we give to our long-term estimation of the outflow. It is in good accordance with the estimates given by *Boutov et al.* [2014] in their numerical analysis of the exchanged flows through the SoG. Therefore, our best estimate of the outflow during the period 2004-2015 is -0.85±0.03 Sv. A very small trend of -4.6×10^{-4} Sv year^{-1} is deduced from the time series, although the regression is not significant at the 95% confidence level. The interface generally shows a specular behavior compared to the outflow. At seasonal scale their phase opposition is evident, reflecting the coincidence of maximum (minimum) outflow with the shallower (deeper) interface in April (September). Their respective spreads also reflect a seasonal periodicity, with maxima in winter (~0.1 Sv and ~7 meters, respectively) and minima in summer (~0.03 Sv and ~4 meters, respectively), surely related to meteorological seasonality, although the interface spread reflects a less pronounced seasonality with respect to the outflow. On the other hand, the relative contribution of the annual amplitude with respect to the means for the interface and the maximum along-strait velocity below the interface is ~2% and ~4%, respectively. Both results suggest that the main source of seasonality for the outflow is the velocity variability and not the interface.

To conclude, we want to mention the sensitivity of our computations to the different steps followed in the data processing. The removal of outliers based on twice the standard deviation of the error of the ensembles (Section 4, Figure 2) modifies the outflow by ~3% with respect to the no exclusion

situation, so that the results are sensitive to this quality control. The application of LoW fit to all the series regardless the RMS residuals threshold, gives slightly higher velocity on average in the bottom layer than the alternative followed in this study of replacing the LoW fit with a linear interpolation in some circumstances (Section 5.4). Such overestimation would yield an outflow increase of ~1%. The effect of a more accurate bathymetry in the flow computations is more important: the mean outflow obtained with the bathymetry by *Zitellini et al.* [2009] is ~6% higher than the one obtained by applying a less precise bathymetry (Table 2). It is in part the same circumstance, along with the use of different numerical outputs to estimate the cross-strait structure, at the origin of the discrepancy between the values presented in this study and the previous ones based on the same dataset, although employing shorter series, provided by *Sánchez Román et al.* [2009], *García Lafuente et al.* [2009] and *Soto Navarro et al.* [2010].

Acknowledgements

The series of current measurements analyzed in this work has been collected during the INGRES Projects, INGRES (REN2003_01608), INGRES2 (CTM2006_02326/MAR) and INGRES3 (CTM2010_21229-C02-01/MAR), and Special Action CTM2009-05810-E/MAR, funded by the Spanish Government. The mooring line is included in the Mediterranean Sea monitoring network of the HYDROCHANGES project sponsored by CIESM. The CTD/LADCP dataset has been provided by the Spanish Oceanographic Institute (IEO) who is coordinate partner of the INGRES3 project. The numerical simulations have been carried out in the framework of the SAMPA project developed in collaboration with the Spanish Port Authority. Partial support has been also provided by projects ENCIBA (CTM2013-40886-P) from the Spanish Government and MOCBASE (RNM1540) from the Junta de Andalucía. We are especially gratefully to the crew of the IEO research vessels 'Odón de Buen', 'Francisco de Paula Navarro', 'Ramón Margalef' and 'Ángeles Alvariño', for the

683 professional execution of the deploy and recover operations of the mooring line. A special thank
684 goes to Miguel, boatswain of R/V Ángeles Alvariño for his kind attention and professional assistance
685 provided onboard. We are also grateful to the anonymous reviewers for their contributions to
686 improve the work. This is the publication no. XX from CEIMAR Publication Series. The complete
687 dataset used in this work is freely available at the following e-mail address:
688 ssammartino@ctima.uma.es.

A. Appendix

Table A-1 – Metadata of the mooring experiments deployed in ES. The field 'Std. dev.' is the theoretical error provided by the initial configuration of the instrument, 'Ping x ensemble' indicates the number of pings used to average the ensemble measurement, 'ADCP avg. depth' is the depth of the ADCP averaged either by linear regression or by the moving average filter, 'Bins' are the number of effective cells retained after the blanking of the out-of-water bins and the application of the sidelobe interference filter, and 'Total drift' stands for the drift of the averaged ADCP depth over the whole duration of the experiment. The experiment CS00 is included for completeness of the series although is not used in this work.

Name	Start time	End time	Duration (days)	ADCP frequency (kHz)	Std. dev. (cm s^{-1})	Ping x ensemble	ADCP avg. depth (m)	Bins	Total drift (m)	Single point currentmeter
ES01	30-Sep-2004	12-Feb-2005	135	75	2.37	28	-346.2	40	0.9	RCM9
ES02	14-Feb-2005	9-Jun-2005	115	75	2.37	28	-342.5	40	0.1	RCM9
ES03	12-Jun-2005	11-Sep-2005	91	75	2.37	28	-340.4	39	0.0	RCM9
ES04	12-Sep-2005	5-Feb-2006	146	75	2.37	28	-346.5	40	-3.0	RCM9
ES05	5-Feb-2006	8-May-2006	92	75	1.37	42	-345.2	40	0.0	RCM9
ES06	8-May-2006	22-Sep-2006	137	75	1.08	50	-343.9	40	-0.2	RCM9*
ES07	23-Sep-2006	28-Jan-2007	127	150	0.93	82	-343.4	36	-5.6	AQD
ES08	11-Feb-2007	18-Jun-2007	127	150	0.93	82	-341.4	36	-6.3	AQD
ES09	19-Jun-2007	29-Oct-2007	132	150	0.94	80	-343.3	36	-3.6	AQD
ES10	29-Oct-2007	24-Mar-2008	147	75	1.34	44	-346.0	40	0.4	AQD*
ES11	25-Mar-2008	10-Jun-2008	77	75	1.34	44	-345.6	40	-0.1	AQD
ES12	11-Jun-2008	8-Oct-2008	119	75	1.34	44	-343.6	40	0.3	AQD
ES13	9-Oct-2008	19-Nov-2008	41	75	1.34	44	-346.7	40	-0.3	AQD
ES14	11-Dec-2008	15-Jan-2009	35	75	1.26	50	-346.2	40	0.4	AQD
ES15	3-Apr-2009	15-Jun-2009	73	75	1.34	44	-346.6	40	0.2	AQD
ES16	15-Jun-2009	11-Oct-2009	118	75	1.34	44	-350.2	41	0.6	AQD
ES17	11-Oct-2009	6-Feb-2010	118	75	2.52	44	-346.3	40	-0.5	AQD*
ES18	6-Feb-2010	9-Jul-2010	153	75	1.34	44	-348.0	40	0.7	AQD
ES19	9-Jul-2010	24-Nov-2010	138	75	1.34	44	-345.3	40	0.0	AQD*
ES20	24-Nov-2010	9-Mar-2011	105	75	1.34	44	-349.6	40	1.7	AQD*
ES21	5-Aug-2011	17-Aug-2011	12	75	1.34	44	-345.3	40	0.3	AQD
CS00	23-Nov-2011	8-Jun-2012	198	75	1.54	57	-282.5	43	-3.1	AQD
ES22	6-Aug-2012	30-Oct-2012	85	75	2.20	44	-340.2	39	0.1	AQD
ES23	1-Nov-2012	6-Jun-2013	217	75	2.20	44	-340.3	39	1.7	AQD*
ES24	8-Jun-2013	26-Sep-2013	110	75	2.37	50	-339.3	39	0.0	AQD
ES25	30-Sep-2013	28-Mar-2014	179	75	2.37	50	-338.6	39	0.3	AQD
ES26	01-Apr-2014	11-Dec-2014	254	75	2.37	50	-338.9	39	-0.5	AQD

ES27	11-Dec-2014	15-Jun-15	186	75	2.07	50	-338.5	39	0.0	AQD

*** For different reasons (loss of the instrument, battery pack failure) data were not collected.**

References

Aanderaa Instruments (2002), RCM9 MkII RCM11 Operating Manual*Rep. 211*, 8-09 pp.

Armi, L., and D. Farmer (1985), The Internal Hydraulics of the Strait of Gibraltar and Associated Sills and Narrows, *Oceanologica Acta*, *8*, 37-46.

Armi, L., and D. M. Farmer (1988), The flow of Mediterranean water through the Strait of Gibraltar, *Progress in Oceanography*, *21*(1), 1-103, doi:http://dx.doi.org/10.1016/0079-6611(88)90055-9.

Baschek, B., U. Send, J. García Lafuente, and J. Candela (2001), Transport estimates in the Strait of Gibraltar with a tidal inverse model, *Journal of Geophysical Research: Oceans*, *106*(C12), 31033-31044, doi:http://dx.doi.org/10.1029/2000JC000458.

Bethoux, J. P. (1979), Budgets of the Mediterranean Sea. Their dependence on the local climate and on the characteristics of the Atlantic waters, *Oceanologica Acta*, *2*, 157-163.

Bormans, M., and C. Garrett (1989), The Effect of Rotation on the Surface Inflow through the Strait of Gibraltar, *Journal of Physical Oceanography*, *19*(10), 1535-1542, doi:http://dx.doi.org/10.1175/1520-0485(1989)019<1535:TEOROT>2.0.CO;2.

Boutov, D., Á. Peliz, P. M. A. Miranda, P. M. M. Soares, R. M. Cardoso, L. Prieto, J. Ruiz, and J. García Lafuente (2014), Inter-annual variability and long term predictability of exchanges through the Strait of Gibraltar, *Global and Planetary Change*, *114*(0), 23-37, doi:http://dx.doi.org/10.1016/j.gloplacha.2013.12.009.

Bray, N. A., J. Ochoa, and T. H. Kinder (1995), The role of the interface in exchange through the Strait of Gibraltar, *Journal of Geophysical Research: Oceans*, *100*(C6), 10755-10776, doi:10.1029/95JC00381.

Bryden, H. L., and H. M. Stommel (1984), Limiting processes that determine basic features of the circulation in the Mediterranean Sea, *Oceanologica Acta*, *7*(3), 289-296.

Bryden, H. L., and T. H. Kinder (1991), Steady two-layer exchange through the Strait of Gibraltar, *Deep Sea Research Part A. Oceanographic Research Papers*, *38, Supplement 1*(0), S445-S463, doi:http://dx.doi.org/10.1016/S0198-0149(12)80020-3.

Bryden, H. L., J. Candela, and T. H. Kinder (1994), Exchange through the Strait of Gibraltar, *Progress in Oceanography*, *33*(3), 201-248, doi:http://dx.doi.org/10.1016/0079-6611(94)90028-0.

Candela, J., C. Winant, and A. Ruiz (1990), Tides in the Strait of Gibraltar, *Journal of Geophysical Research: Oceans*, *95*(C5), 7313-7335, doi:http://dx.doi.org/10.1029/JC095iC05p07313.

Candela, J. (2001), Mediterranean water and global circulation, in *Ocean Circulation and Climate Observing and Modelling the Global Ocean*, edited by G. Siedler, J. Gould and J. Church, p. 715, Academic Press

Carter, D. B. (1956), The water balance of the Mediterranean and Black Seas, *Climatology Drexel Institute of Technology, Laboratory of Climatology*, *9*, 123-175.

Foken, T., M. Aubinet, and R. Leuning (2012), The Eddy Covariance Method, in *Eddy Covariance*, edited by M. Aubinet, T. Vesala and D. Papale, pp. 1-19, Springer Netherlands, doi:10.1007/978-94-007-2351-1_1.

García Lafuente, J., J. M. Vargas, F. Plaza, T. Sarhan, J. Candela, and B. Bascheck (2000), Tide at the eastern section of the Strait of Gibraltar, *Journal of Geophysical Research: Oceans*, *105*(C6), 14197-14213, doi:http://dx.doi.org/10.1029/2000JC900007.

García Lafuente, J., E. Álvarez Fanjul, J. M. Vargas, and A. W. Ratsimandresy (2002), Subinertial variability in the flow through the Strait of Gibraltar, *Journal of Geophysical Research: Oceans*, *107*(C10), 3168, doi:http://dx.doi.org/10.1029/2001JC001104.

García Lafuente, J., A. Sánchez Román, G. Díaz del Río, G. Sannino, and J. C. Sánchez Garrido (2007), Recent observations of seasonal variability of the Mediterranean outflow in the Strait of Gibraltar, *Journal of Geophysical Research: Oceans*, *112*(C10), C10005, doi:http://dx.doi.org/10.1029/2006JC003992.

García Lafuente, J., J. Delgado, A. Sánchez Román, J. Soto, L. Carracedo, and G. Díaz del Río (2009), Interannual variability of the Mediterranean outflow observed in Espartel sill, western Strait of Gibraltar, *Journal of Geophysical Research: Oceans*, *114*(C10), C10018, doi:http://dx.doi.org/10.1029/2009JC005496.

García Lafuente, J., A. Sánchez Román, C. Naranjo, and J. C. Sánchez Garrido (2011), The very first transformation of the Mediterranean outflow in the Strait of Gibraltar, *Journal of Geophysical Research: Oceans*, *116*(C7), C07010, doi:http://dx.doi.org/10.1029/2011JC006967.

García Lafuente, J., E. Bruque Pozas, J. C. Sánchez Garrido, G. Sannino, and S. Sammartino (2013), The interface mixing layer and the tidal dynamics at the eastern part of the Strait of Gibraltar, *Journal of Marine Systems*, *117–118*(0), 31-42, doi:http://dx.doi.org/10.1016/j.jmarsys.2013.02.014.

Garrett, C. J. R., and W. H. Munk (1971), The age of the tide and the "Q" of the oceans, *Deep Sea Research and Oceanographic Abstracts*, *18*(5), 493-503, doi:http://dx.doi.org/10.1016/0011-7471(71)90073-8.

Izquierdo, F. J., M. Estareas, and N. G. Sandoval (1996), Depósitos coralinos litificados en el Estrecho de Gibraltar, *Geogaceta*, *20*(2), 401-404.

Johnson, G. C., R. G. Lueck, and T. B. Sanford (1994), Stress on the Mediterranean Outflow Plume: Part II. Turbulent Dissipation and Shear Measurements, *Journal of Physical Oceanography*, *24*(10), 2084-2092, doi:http://dx.doi.org/10.1175/1520-0485(1994)024<2084:SOTMOP>2.0.CO;2.

Kundu, P. K. (1976), Ekman Veering Observed near the Ocean Bottom, *Journal of Physical Oceanography*, *6*(2), 238-242, doi:http://dx.doi.org/10.1175/1520-0485(1976)006<0238:EVONTO>2.0.CO;2.

Kundu, P. K., and I. M. Cohen (2004), *Fluid Mechanics*, Elsevier Science.

Lacombe, H., and C. Richez (1982), The Regime of the Strait of Gibraltar, in *Elsevier Oceanography Series*, edited by C. J. N. Jacques, pp. 13-73, Elsevier, doi:http://dx.doi.org/10.1016/S0422-9894(08)71237-6.

Naranjo, C., J. Garcia Lafuente, G. Sannino, and J. C. Sanchez Garrido (2014), How much do tides affect the circulation of the Mediterranean Sea? From local processes in the Strait of Gibraltar to basin-scale effects, *Progress in Oceanography*(0), doi:http://dx.doi.org/10.1016/j.pocean.2014.06.005.

New, A. L., S. Barnard, P. Herrmann, and J. M. Molines (2001), On the origin and pathway of the saline inflow to the Nordic Seas: insights from models, *Progress in Oceanography*, *48*(2–3), 255-287, doi:http://dx.doi.org/10.1016/S0079-6611(01)00007-6.

Nielsen, J. N. (1912), *Hydrography of the Mediterranean and Adjacent Waters*.

Peliz, A., D. Boutov, R. M. Cardoso, J. Delgado, and P. M. M. Soares (2013), The Gulf of Cadiz–Alboran Sea sub-basin: Model setup, exchange and seasonal variability, *Ocean Modelling*, *61*(0), 49-67, doi:http://dx.doi.org/10.1016/j.ocemod.2012.10.007.

Perlin, A., J. N. Moum, J. M. Klymak, M. D. Levine, T. Boyd, and P. M. Kosro (2005), A modified law-of-the-wall applied to oceanic bottom boundary layers, *Journal of Geophysical Research: Oceans*, *110*(C10), C10S10, doi:http://dx.doi.org/10.1029/2004JC002310.

Plimpton, P. E., H. P. Freitag, and M. J. McPhaden (2004), Processing of Subsurface ADCP Data in the Equatorial Pacific*Rep. OAR PMEL-125*.

Pond, S., and G. L. Pickard (1983), *Introductory Dynamical Oceanography*, 2nd ed., 329 pp., Butterworth-Heinemann.

Rahmstorf, S. (1998), Influence of Mediterranean Outflow on climate, *Eos, Transactions American Geophysical Union*, *79*(24), 281-282, doi:http://dx.doi.org/10.1029/98EO00208.

Reid, J. L. (1979), On the contribution of the Mediterranean Sea outflow to the Norwegian-Greenland Sea, *Deep Sea Research Part A. Oceanographic Research Papers*, *26*(11), 1199-1223, doi:http://dx.doi.org/10.1016/0198-0149(79)90064-5.

Rogerson, M., E. J. Rohling, and P. P. E. Weaver (2006), Promotion of meridional overturning by Mediterranean-derived salt during the last deglaciation, *Paleoceanography*, *21*(4), PA4101, doi:http://dx.doi.org/10.1029/2006PA001306.

Sammartino, S., J. García Lafuente, J. C. Sánchez Garrido, F. J. De los Santos, E. Álvarez Fanjul, C. Naranjo, M. Bruno, and C. Calero (2014), A numerical model analysis of the tidal flows in the Bay of Algeciras, Strait of Gibraltar, *Continental Shelf Research*, *72*(0), 34-46, doi:http://dx.doi.org/10.1016/j.csr.2013.11.002.

Sánchez Garrido, J. C., G. Sannino, L. Liberti, J. García Lafuente, and L. Pratt (2011), Numerical modeling of three-dimensional stratified tidal flow over Camarinal Sill, Strait of Gibraltar, *Journal of Geophysical Research: Oceans*, *116*(C12), C12026, doi:http://dx.doi.org/10.1029/2011JC007093.

Sánchez Garrido, J. C., J. García Lafuente, E. Álvarez Fanjul, M. G. Sotillo, and F. J. de los Santos (2013), What does cause the collapse of the Western Alboran Gyre? Results of an operational ocean model, *Progress in Oceanography*, *116*(0), 142-153, doi:http://dx.doi.org/10.1016/j.pocean.2013.07.002.

Sánchez Garrido, J. C., J. G. Lafuente, S. Sammartino, C. Naranjo, F. J. de los Santos, and E. Álvarez Fanjul (2014), Meteorologically-driven circulation and flushing times of the Bay of Algeciras, Strait of Gibraltar, *Marine Pollution Bulletin*, *80*(1–2), 97-106, doi:http://dx.doi.org/10.1016/j.marpolbul.2014.01.036.

Sánchez Román, A., F. Criado Aldeanueva, J. García Lafuente, and J. C. Sánchez Garrido (2008), Vertical structure of tidal currents over Espartel and Camarinal sills, Strait of Gibraltar, *Journal of Marine Systems*, *74*(1–2), 120-133, doi:http://dx.doi.org/10.1016/j.jmarsys.2007.11.007.

Sánchez Román, A., G. Sannino, J. García Lafuente, A. Carillo, and F. Criado Aldeanueva (2009), Transport estimates at the western section of the Strait of Gibraltar: A combined experimental and numerical modeling study, *Journal of Geophysical Research: Oceans*, *114*(C6), C06002, doi:http://dx.doi.org/10.1029/2008JC005023.

Sánchez Román, A., J. García Lafuente, J. Delgado, J. C. Sánchez Garrido, and C. Naranjo (2012), Spatial and temporal variability of tidal flow in the Strait of Gibraltar, *Journal of Marine Systems*, *98–99*(0), 9-17, doi:http://dx.doi.org/10.1016/j.jmarsys.2012.02.011.

Sannino, G., A. Bargagli, and V. Artale (2004), Numerical modeling of the semidiurnal tidal exchange through the Strait of Gibraltar, *Journal of Geophysical Research: Oceans*, *109*(C5), C05011, doi:http://dx.doi.org/10.1029/2003JC002057.

Sannino, G., A. Carillo, and V. Artale (2007), Three-layer view of transports and hydraulics in the Strait of Gibraltar: A three-dimensional model study, *Journal of Geophysical Research: Oceans*, *112*(C3), C03010, doi:http://dx.doi.org/10.1029/2006JC003717.

Sannino, G., L. Pratt, and A. Carillo (2009), Hydraulic Criticality of the Exchange Flow through the Strait of Gibraltar, *Journal of Physical Oceanography*, *39*(11), 2779-2799, doi:http://dx.doi.org/10.1175/2009JPO4075.1.

Schott, G. (1915), Die Gewasser des Mittelmeeres, *Annalen der Hydrographie und Maritimen Meteorologie*, *43*, 63-79.

Soto Navarro, J., F. Criado Aldeanueva, J. García Lafuente, and A. Sánchez Román (2010), Estimation of the Atlantic inflow through the Strait of Gibraltar from climatological and in situ data, *Journal of Geophysical Research: Oceans*, *115*(C10), C10023, doi:http://dx.doi.org/10.1029/2010JC006302.

Stewart, R. H. (2009), *Introduction to Physical Oceanography*, 345 pp., Orange Grove Books.

Sverdrup, H. U., M. W. Johnson, and R. H. Fleming (1942), *The Oceans, Their Physics, Chemistry, and General Biology*, 1087 pp., Prentice-Hall, New York.

Teledyne RD Instruments (2010), ADCP Coordinate Transformation Formulas and Calculations*Rep. P/N 951-6079-00*, 32 pp.

Teledyne RD Instruments (2011), Acoustic Doppler Current Profiler Principles of Operation A Practical Primer*Rep. P/N 951-6069-00*, 56 pp.

Teledyne RD Instruments (2013a), Workhorse Monitor, Sentinel, Mariner, Long Ranger and Quartermaster commands and output data format*Rep. P/N 957-6156-00*, 176 pp.

Teledyne RD Instruments (2013b), Long Ranger & QuarterMaster Operation Manual*Rep. P/N 957-6269-00*, 176 pp.

Thorpe, S. A. (2007), *An Introduction to Ocean Turbulence*, 240 pp., Cambridge University Press.

837 Tsimplis, M. N., and H. L. Bryden (2000), Estimation of the transports through the Strait of Gibraltar, *Deep*
838 *Sea Research Part I: Oceanographic Research Papers*, *47*(12), 2219-2242,
839 doi:http://dx.doi.org/10.1016/S0967-0637(00)00024-8.

840 Vargas, J. M., J. García Lafuente, J. Candela, and A. J. Sánchez (2006), Fortnightly and monthly variability
841 of the exchange through the Strait of Gibraltar, *Progress in Oceanography*, *70*(2–4), 466-485,
842 doi:http://dx.doi.org/10.1016/j.pocean.2006.07.001.

843 Zitellini, N., et al. (2009), The quest for the Africa–Eurasia plate boundary west of the Strait of Gibraltar,
844 *Earth and Planetary Science Letters*, *280*(1–4), 13-50, doi:http://dx.doi.org/10.1016/j.epsl.2008.12.005.

845

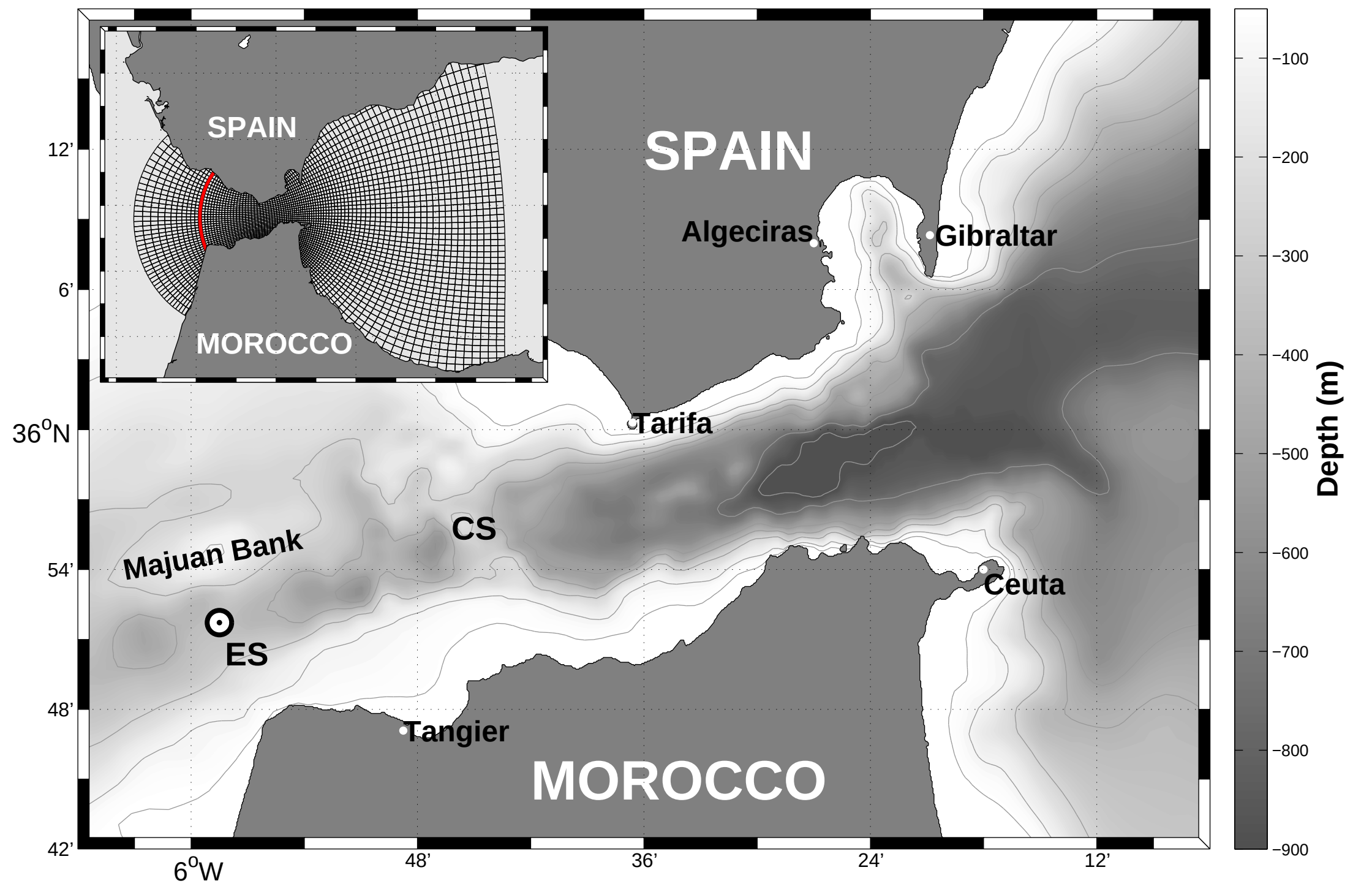
SPAIN
MOROCCO
SPAIN
Algeciras
Gibraltar
Tarifa
CS
Majuan Bank
ES
Ceuta
Tangier
MOROCCO
12’
6’
36°N
54’
48’
42’
6°W
48’
36’
24’
12’
Depth (m)
−100
−200
−300
−400
−500
−600
−700
−800
−900

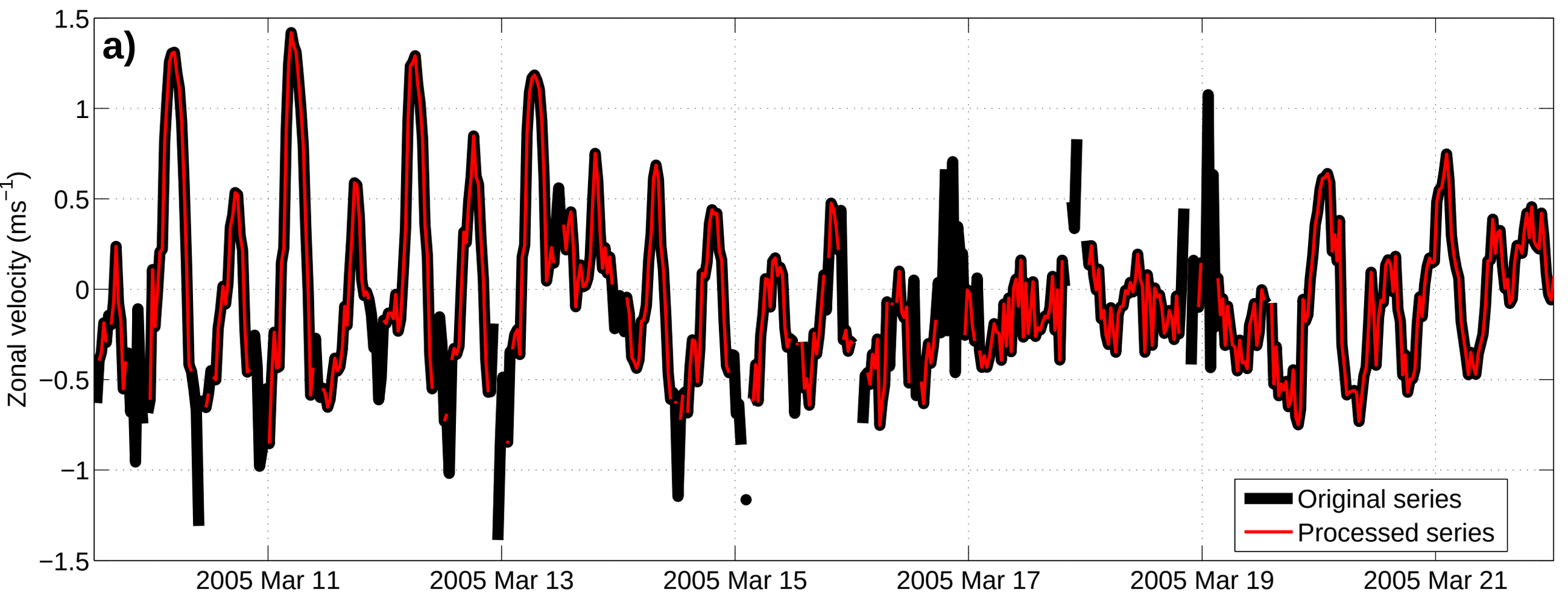
a)
1.5
1
0.5
0
−0.5
−1
−1.5
Zonal velocity (ms^{-1})
2005 Mar 11
2005 Mar 13
2005 Mar 15
2005 Mar 17
2005 Mar 19
2005 Mar 21
Original series
Processed series

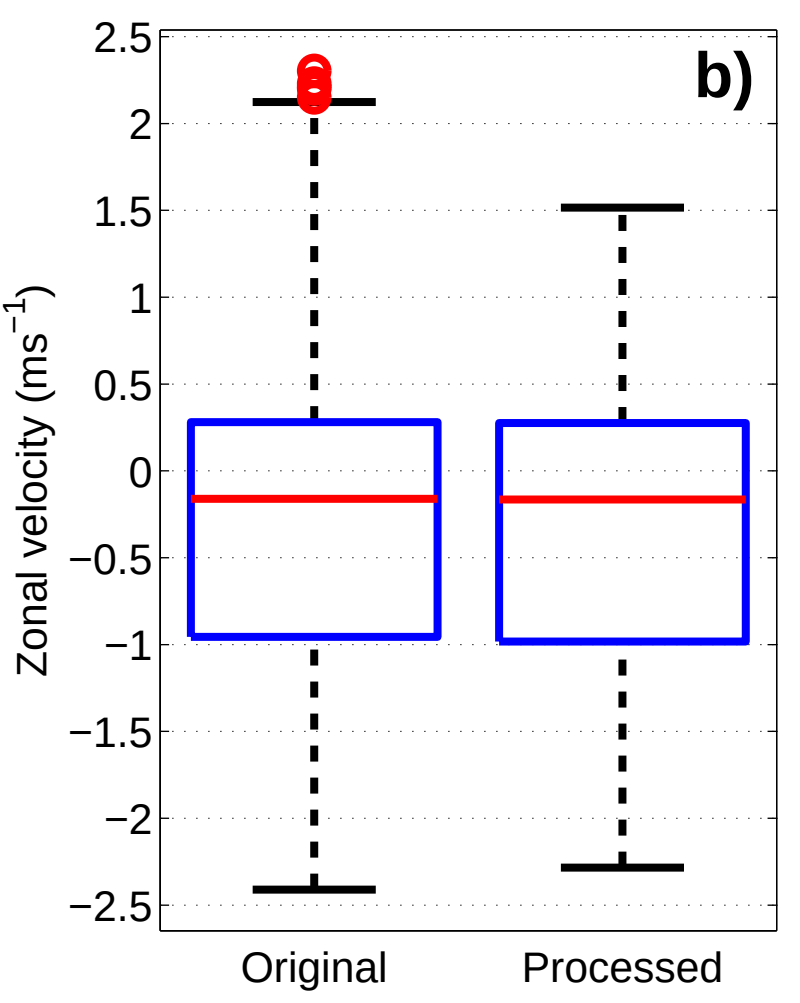
b)
Zonal velocity (ms^{-1})
2.5
2
1.5
1
0.5
0
−0.5
−1
−1.5
−2
−2.5
Original
Processed

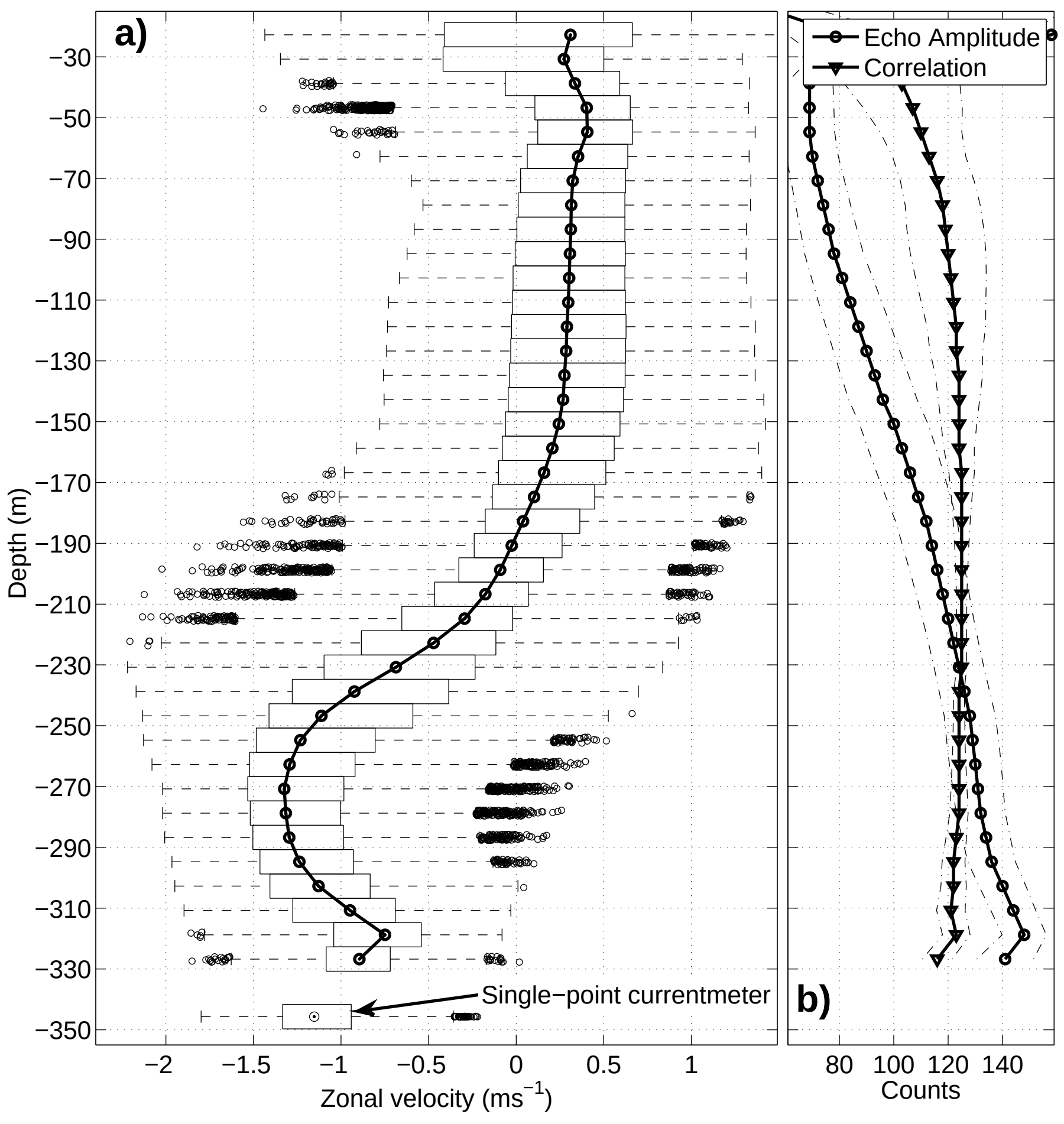
a)
b)
Depth (m)
−30
−50
−70
−90
−110
−130
−150
−170
−190
−210
−230
−250
−270
−290
−310
−330
−350
−2
−1.5
−1
−0.5
0
0.5
1
Zonal velocity (ms^{-1})
Single−point currentmeter
Echo Amplitude
Correlation
80
100
120
140
Counts

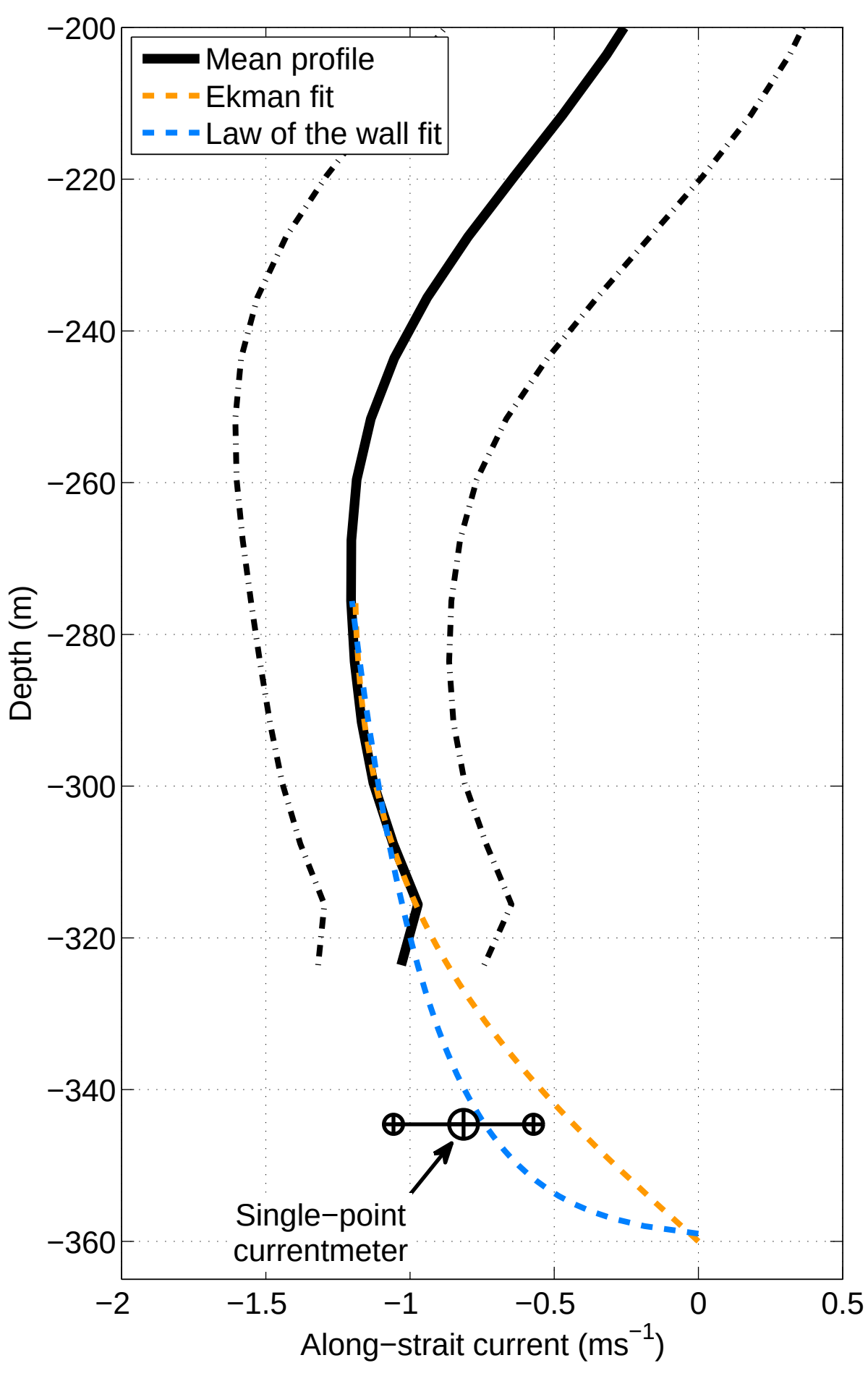
Mean profile
Ekman fit
Law of the wall fit
Single−point
currentmeter
Depth (m)
−200
−220
−240
−260
−280
−300
−320
−340
−360
−2
−1.5
−1
−0.5
0
0.5
Along−strait current (ms^{-1})

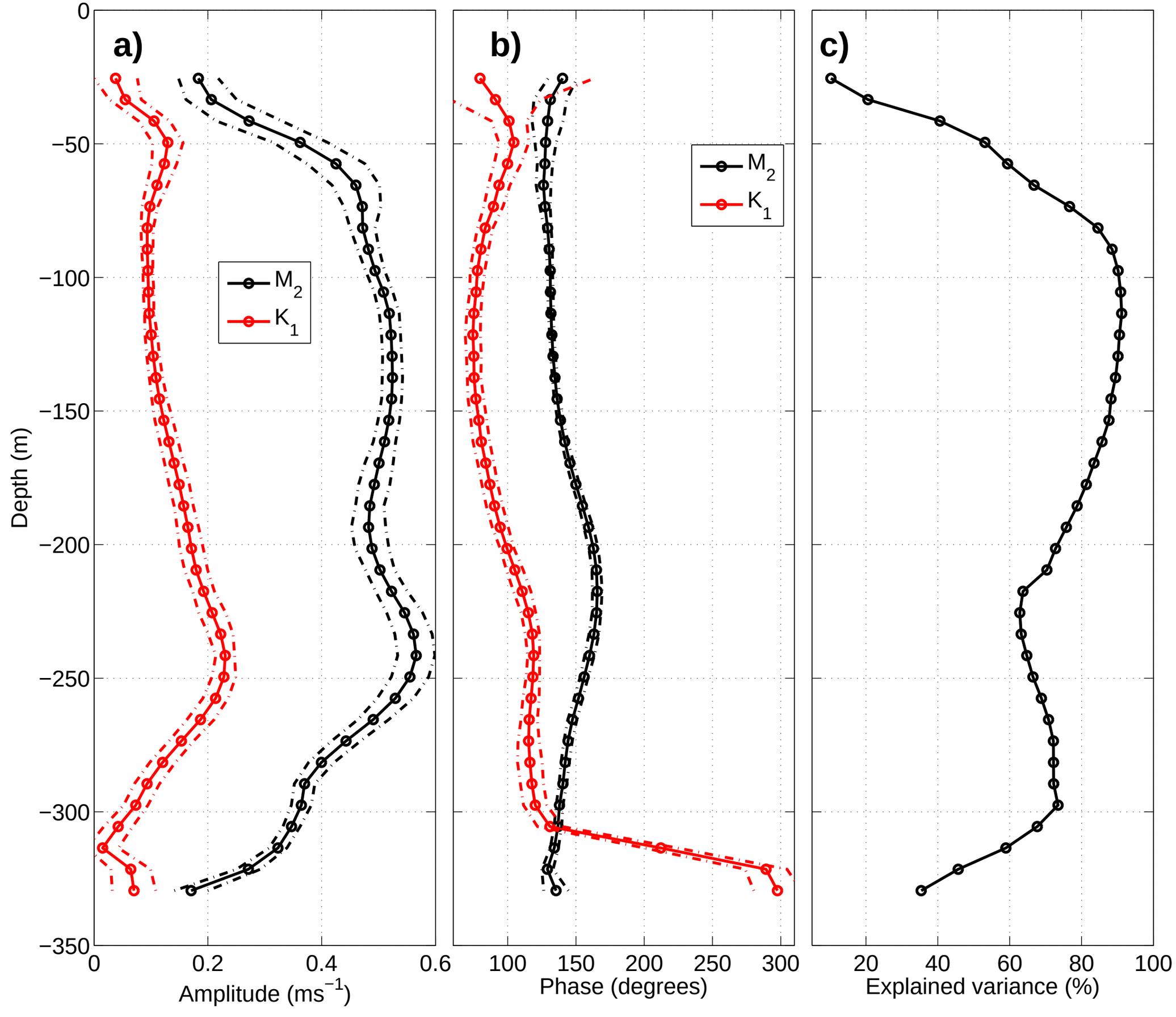
a)
b)
c)
M2
K1
Depth (m)
0
−50
−100
−150
−200
−250
−300
−350
0
0.2
0.4
0.6
Amplitude (ms−1)
100
150
200
250
300
Phase (degrees)
20
40
60
80
100
Explained variance (%)

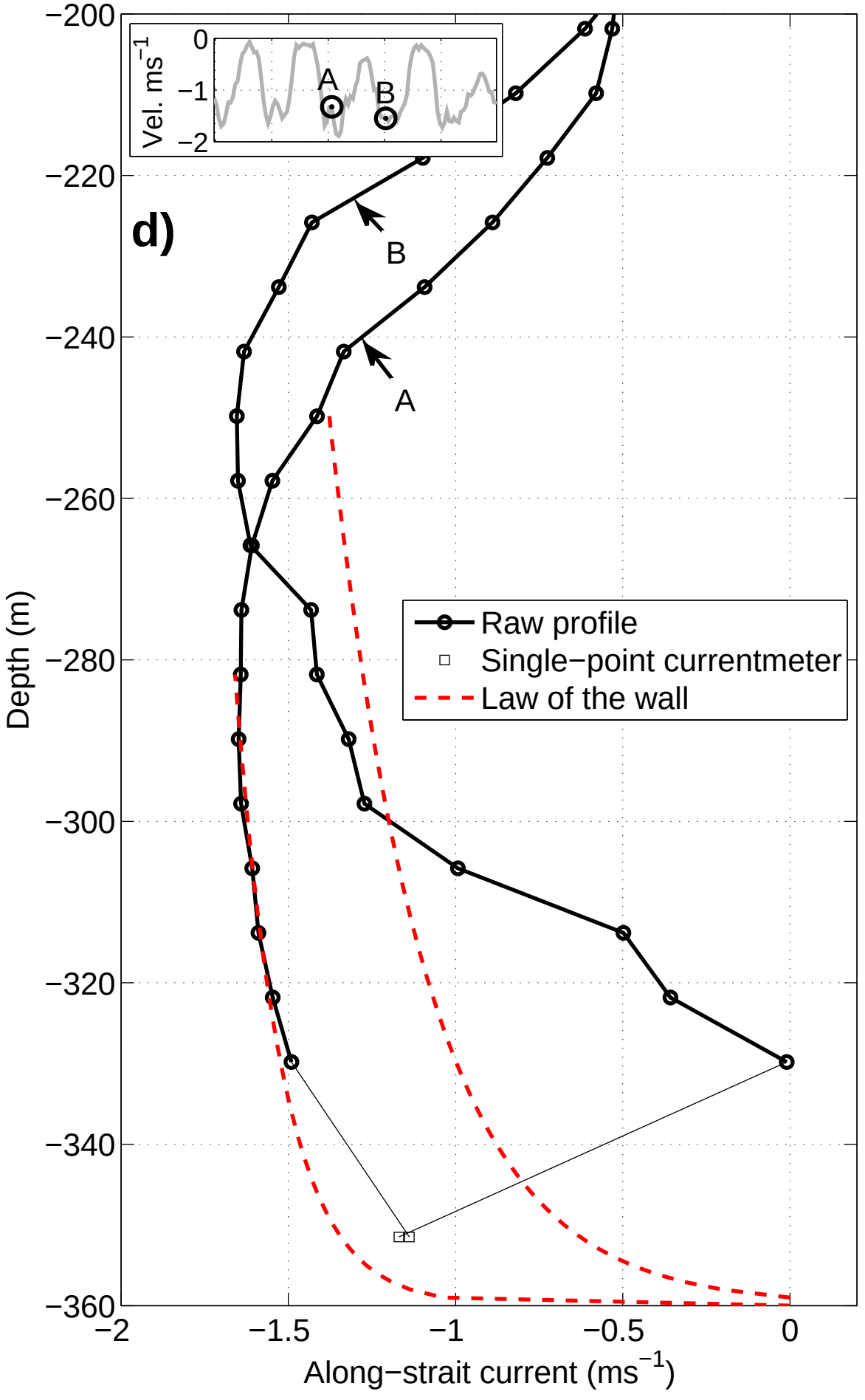
d)
Vel. ms^{-1}
0
−1
−2
A
B
B
A
Raw profile
Single−point currentmeter
Law of the wall
Depth (m)
−200
−220
−240
−260
−280
−300
−320
−340
−360
−2
−1.5
−1
−0.5
0
Along−strait current (ms^{-1})

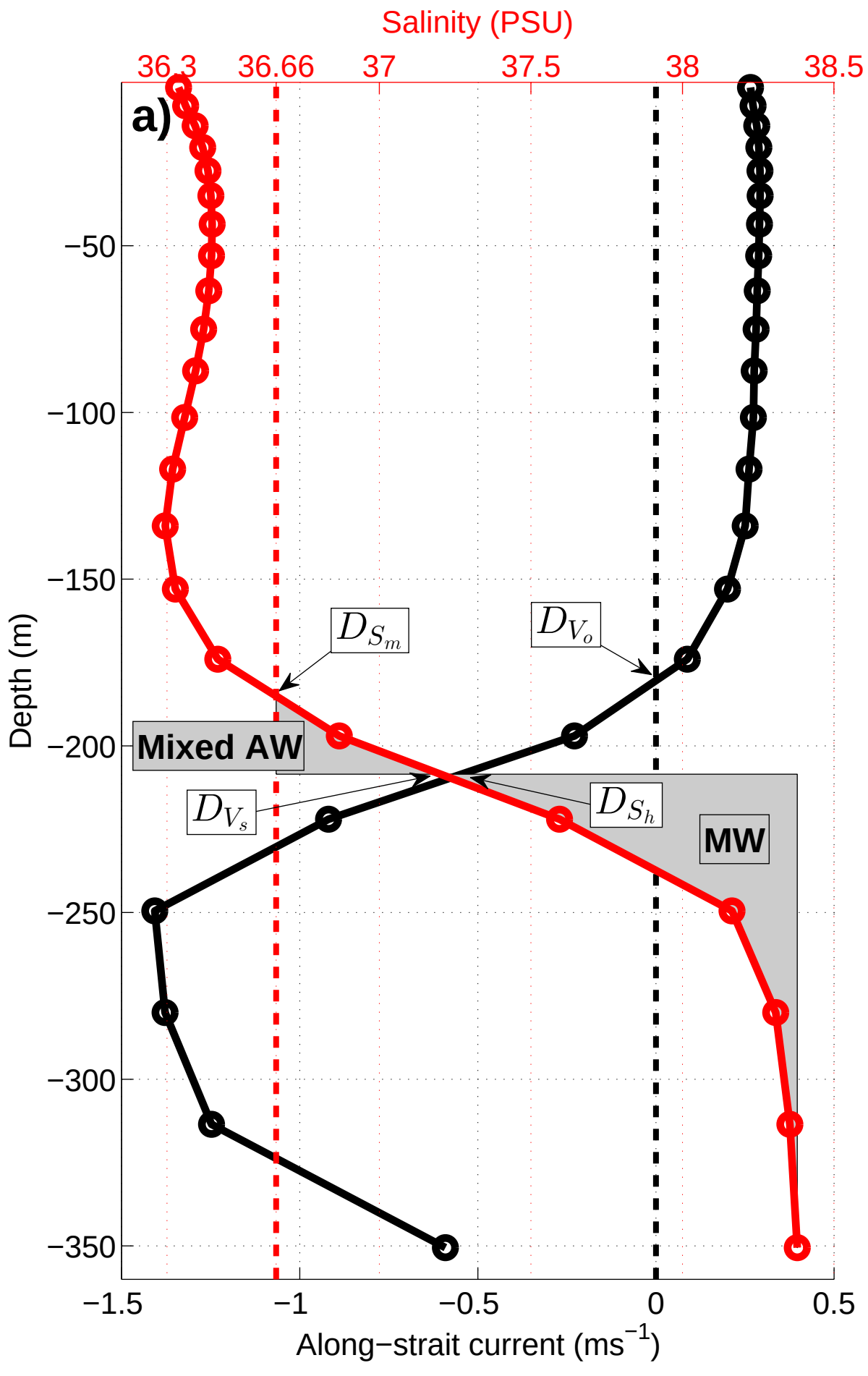
Salinity (PSU)
36.3
36.66
37
37.5
38
38.5
a)
−50
−100
−150
−200
−250
−300
−350
Depth (m)
D_{S_m}
D_{V_o}
Mixed AW
D_{V_s}
D_{S_h}
MW
−1.5
−1
−0.5
0
0.5
Along−strait current (ms^{-1})

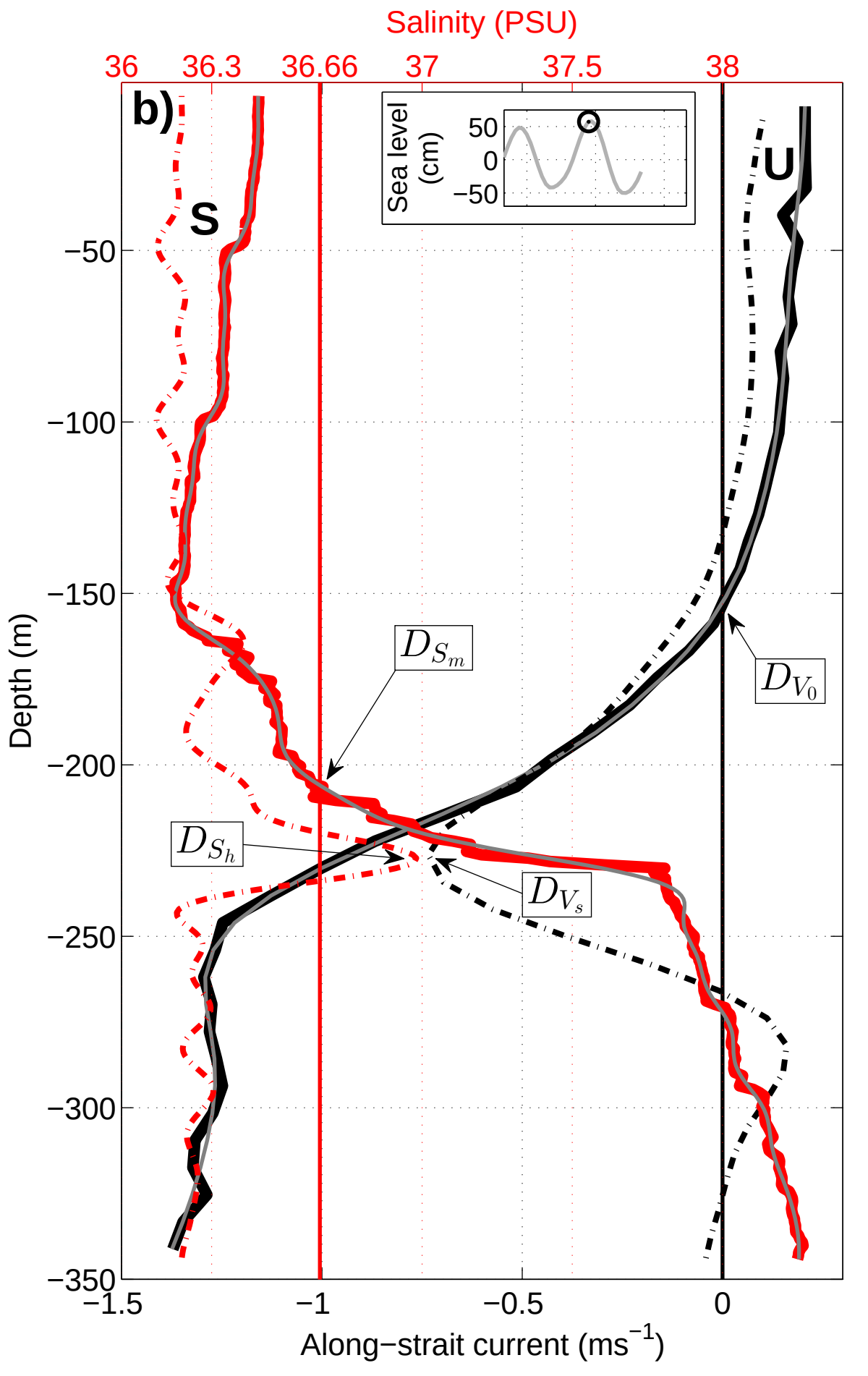
Salinity (PSU)
36
36.3
36.66
37
37.5
38
b)
S
U
Sea level (cm)
50
0
−50
−50
−100
−150
−200
−250
−300
−350
Depth (m)
D_{S_m}
D_{V_0}
D_{S_h}
D_{V_s}
−1.5
−1
−0.5
0
Along−strait current (ms^{-1})

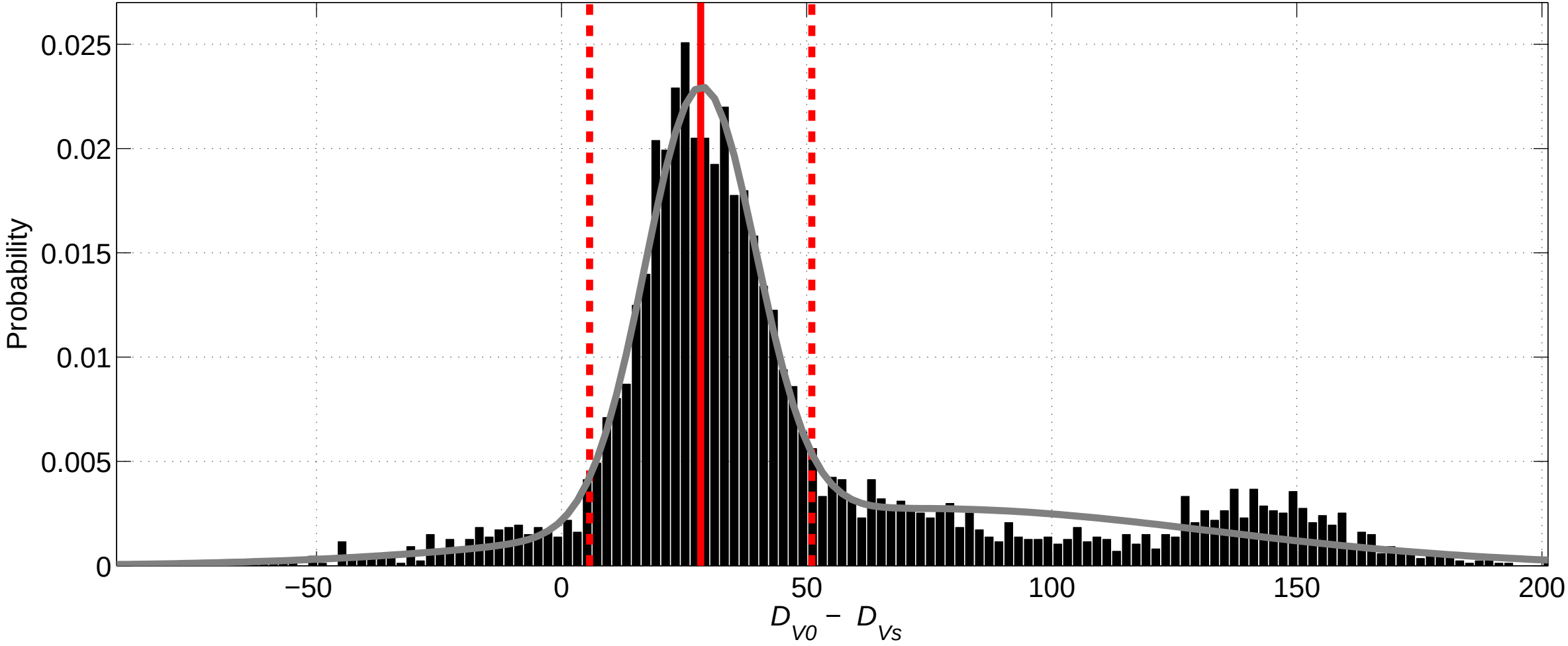
0.025
0.02
0.015
0.01
0.005
0
Probability
−50
0
50
100
150
200
$D_{V0} - D_{Vs}$

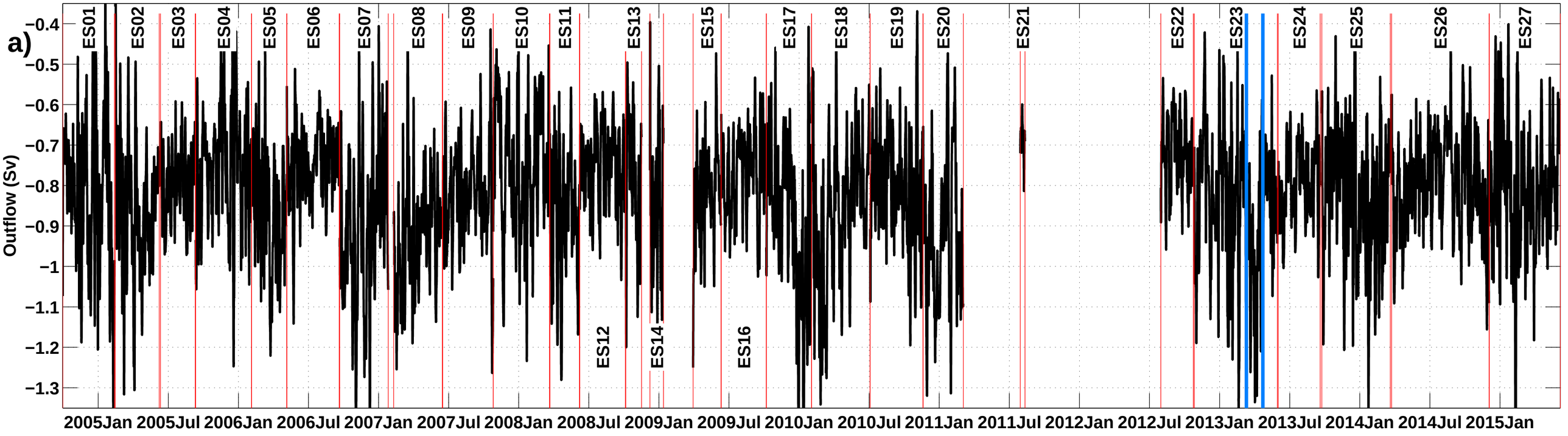
a)
Outflow (Sv)
−0.4
−0.5
−0.6
−0.7
−0.8
−0.9
−1
−1.1
−1.2
−1.3
ES01
ES02
ES03
ES04
ES05
ES06
ES07
ES08
ES09
ES10
ES11
ES12
ES13
ES14
ES15
ES16
ES17
ES18
ES19
ES20
ES21
ES22
ES23
ES24
ES25
ES26
ES27
2005Jan
2005Jul
2006Jan
2006Jul
2007Jan
2007Jul
2008Jan
2008Jul
2009Jan
2009Jul
2010Jan
2010Jul
2011Jan
2011Jul
2012Jan
2012Jul
2013Jan
2013Jul
2014Jan
2014Jul
2015Jan

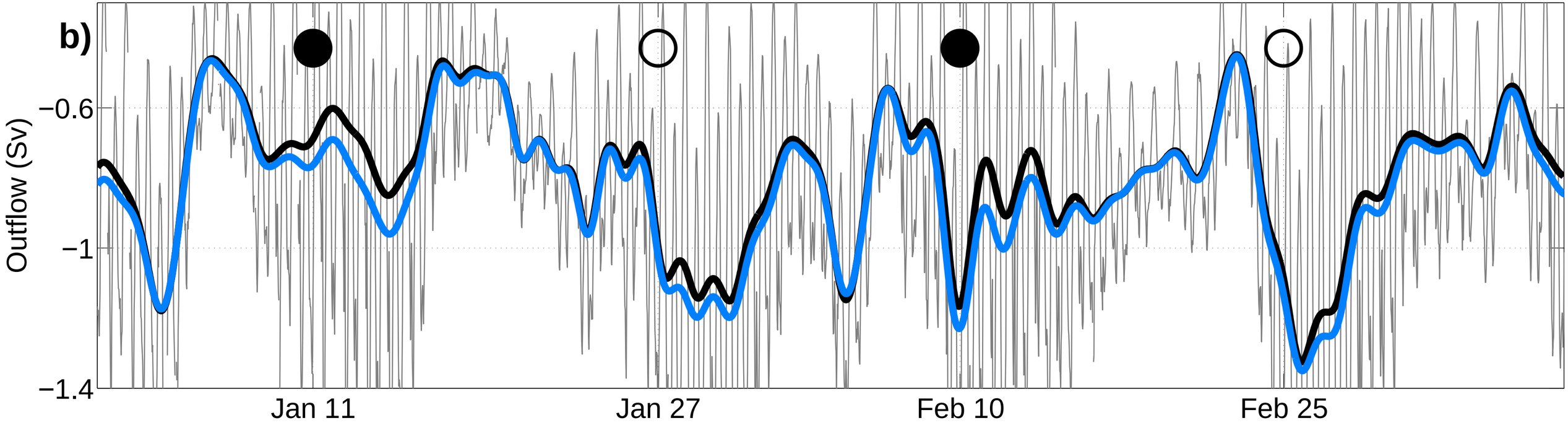
b)
Outflow (Sv)
−0.6
−1
−1.4
Jan 11
Jan 27
Feb 10
Feb 25

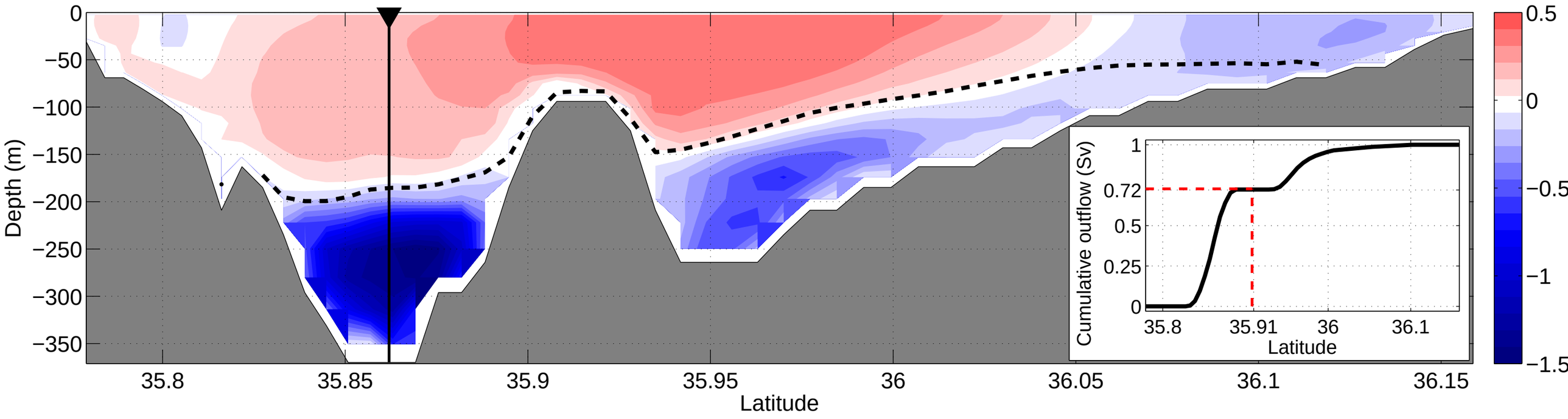
Depth (m)
0
−50
−100
−150
−200
−250
−300
−350
35.8
35.85
35.9
35.95
36
36.05
36.1
36.15
Latitude
0.5
0
−0.5
−1
−1.5
Cumulative outflow (Sv)
1
0.72
0.5
0.25
0
35.8
35.91
36
36.1
Latitude

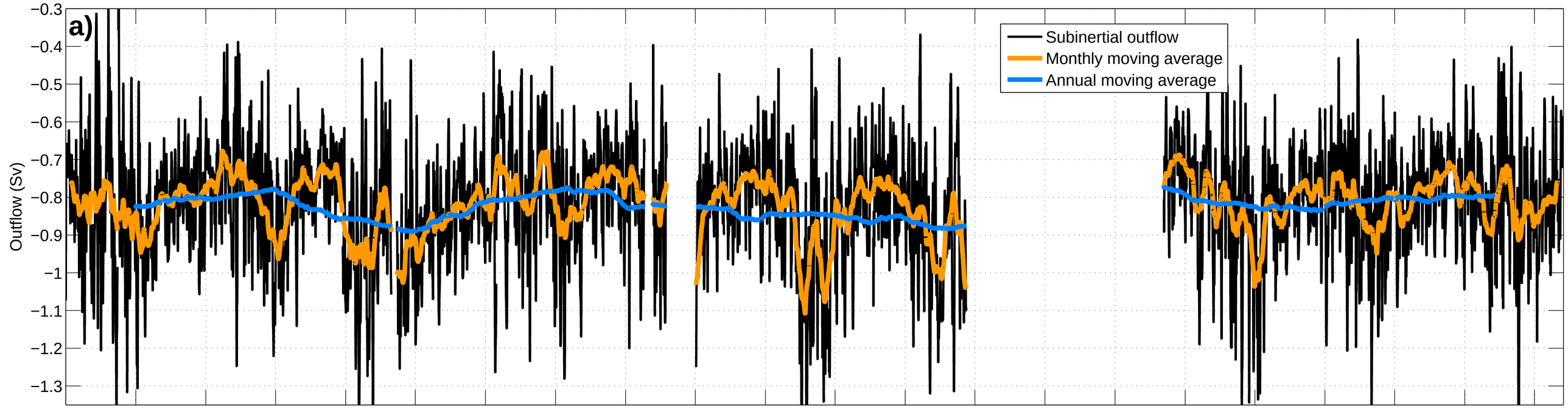
a)
Outflow (Sv)
−0.3
−0.4
−0.5
−0.6
−0.7
−0.8
−0.9
−1
−1.1
−1.2
−1.3
Subinertial outflow
Monthly moving average
Annual moving average

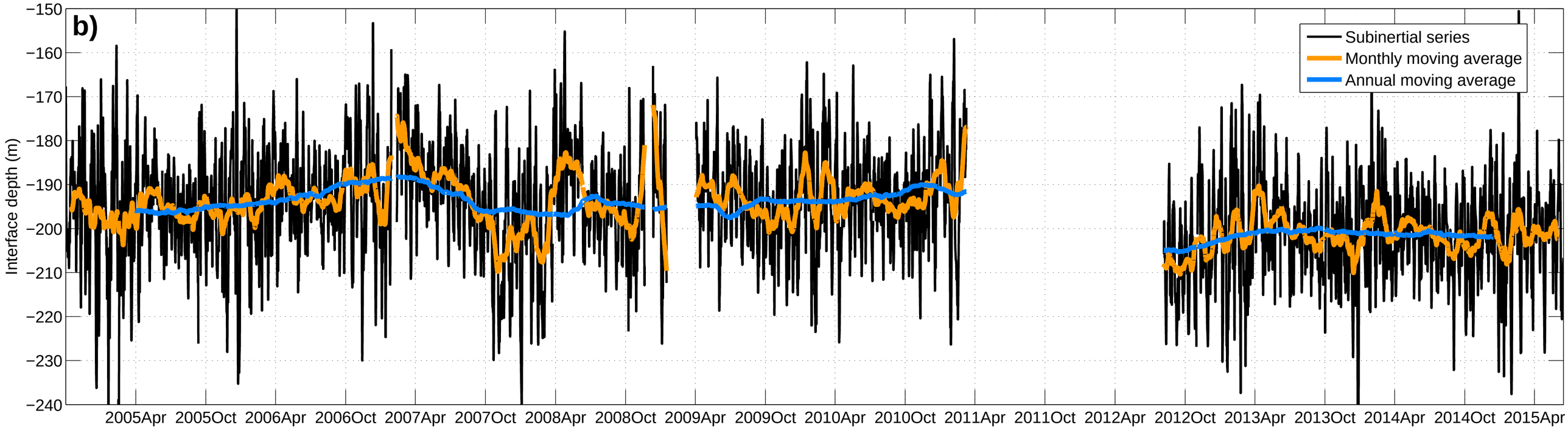
b)
Subinertial series
Monthly moving average
Annual moving average
Interface depth (m)
−150
−160
−170
−180
−190
−200
−210
−220
−230
−240
2005Apr
2005Oct
2006Apr
2006Oct
2007Apr
2007Oct
2008Apr
2008Oct
2009Apr
2009Oct
2010Apr
2010Oct
2011Apr
2011Oct
2012Apr
2012Oct
2013Apr
2013Oct
2014Apr
2014Oct
2015Apr

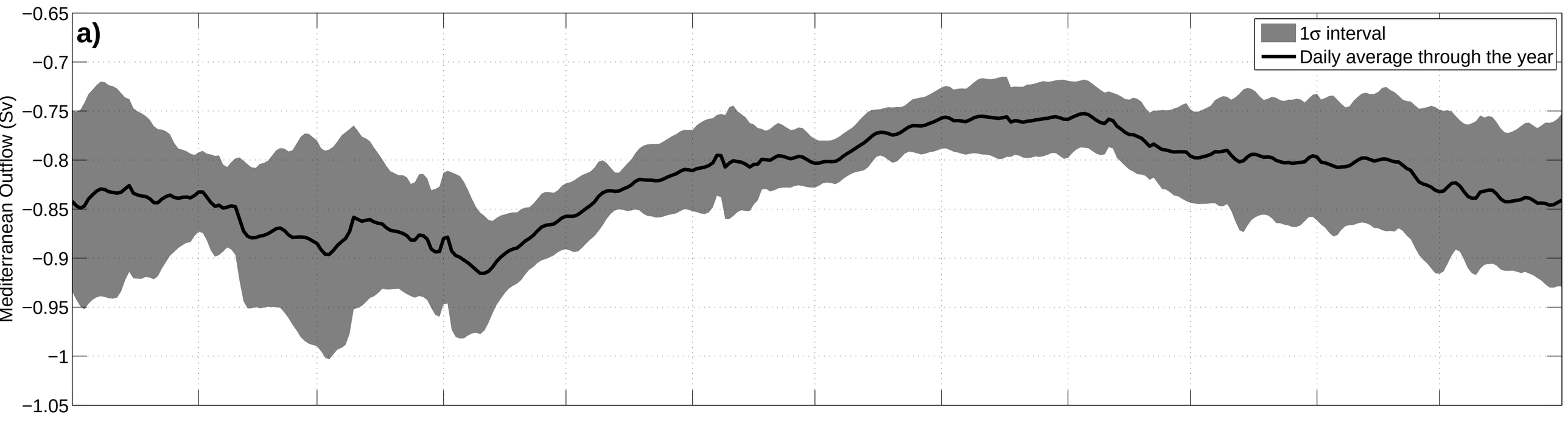
a)
1σ interval
Daily average through the year
Mediterranean Outflow (Sv)
−0.65
−0.7
−0.75
−0.8
−0.85
−0.9
−0.95
−1
−1.05

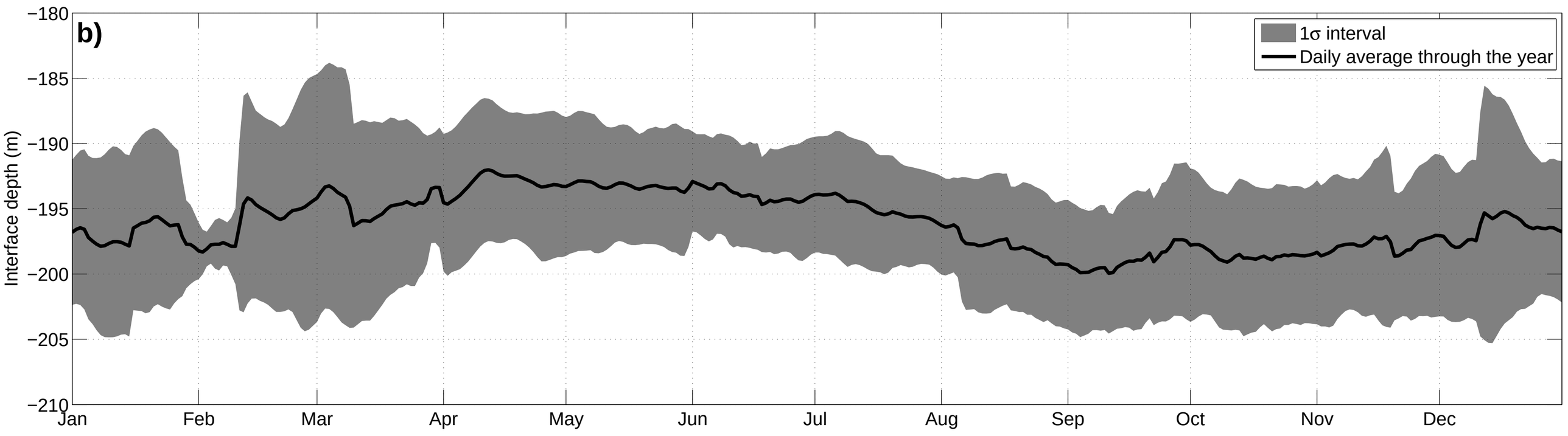
b)
1σ interval
Daily average through the year
Interface depth (m)
−180
−185
−190
−195
−200
−205
−210
Jan
Feb
Mar
Apr
May
Jun
Jul
Aug
Sep
Oct
Nov
Dec